

Chaos in a 3-body Self-Gravitating Cosmological Spacetime

M.J. Koop¹, R.B. Mann²,

Dept. of Physics, University of Waterloo Waterloo, ONT N2L 3G1, Canada

S. Bachmann³

Institute for Theoretical Physics, ETH Zurich, 8093 Zurich, Switzerland

PACS numbers: 13.15.-f, 14.60.Gh, 04.80.+z

September 26, 2018

Abstract

We investigate the equal-mass 3-body system in general relativistic linear gravity in the presence of a cosmological constant Λ . The cosmological vacuum energy introduces features that do not have a non-relativistic counterpart, inducing a competing expansion/contraction of spacetime that competes with the gravitational self-attraction of the bodies. We derive a canonical expression for the Hamiltonian of the system and discuss the numerical solution of the resulting equations of motion. As for the system with $\Lambda = 0$, we find that the structure of the phase space yields a rich variety of interesting dynamics that can be divided into three distinct regions: annulus, pretzel, and chaotic; the first two being regions of quasi-periodicity while the latter is a region of chaos. However unlike the $\Lambda = 0$ case, we find that a negative cosmological constant considerably diminishes the amount of chaos in the system, even beyond that of the $\Lambda = 0$ non-relativistic system. By contrast, a positive cosmological constant considerably enhances the amount of chaos, typically leading to KAM breakdown.

¹email: mjkoop@sciborg.uwaterloo.ca

²email: rbmann@sciborg.uwaterloo.ca

³email: svenb@phys.ethz.ch

1 INTRODUCTION

The N-body problem – that of describing the motion of a system of N particles interacting through specified forces – is one of the oldest problems in physics. Even now it continues to be a problem in fields ranging from nuclear physics to stellar evolution and cosmology. When the problem is that of N particles interacting through their mutual gravitational attraction it is particularly challenging. In the Newtonian case in three spatial dimensions, an exact solution is only known for the N=2 case, and for the general relativistic case in three spatial dimensions there is no exact solution for the equations of motion for even the N=2 case (although approximation techniques exist [1]). This is largely due to the dissipation of energy in the form of gravitational radiation, which results in the system needing to be solved by approximate solutions.

Considerable progress has been made in recent years by studying systems with reduced spatial dimensions. Nonrelativistic one-dimensional self-gravitating systems (OGS) of N particles have been very important in the fields of astrophysics and cosmology for over 30 years [2]. Although they are primarily used as prototypes for studying gravity in higher dimensions, there are physical systems with dynamics closely approximated by the one dimensional system. Very long-lived core-halo configurations, reminiscent of structures observed in globular clusters, are known to exist in the OGS phase space [3]. These model a dense massive core in near-equilibrium, surrounded by a halo of high kinetic energy stars that interact only weakly with the core. Also, the collisions of flat parallel domain walls moving in a direction perpendicular to their surfaces and the dynamics of stars in a direction orthogonal to the plane of a highly flattened galaxy are approximated by the OGS system.

In this paper we continue an ongoing investigation into relativistic one-dimensional self-gravitating systems (ROGSs). This is carried out in the context of a (1+1)-dimensional theory of gravity (lineal gravity) that models (3+1) general relativity by setting the Ricci scalar R equal to the trace of the stress energy of prescribed matter fields and sources. For the ROGS these sources are point particles minimally coupled to gravity. Hence, as in (3+1) dimensions, the evolution of space-time curvature is governed by the matter distribution, which in turn is governed by the dynamics of space-time [4]. Referred to as $R = T$ theory, it is a particular member of a class of dilaton gravity theories on a line. What makes this theory of particular interest is that it has a consistent nonrelativistic ($c \rightarrow \infty$) limit [4] (a problem for generic (1+1)-dimensional gravity [5]), and in this limit reduces to the Newtonian OGS as a special case. Furthermore, when the stress energy is that of a cosmological constant, it reduces to Jackiw-Teitelboim theory [6].

The three body ROGS has been studied previously and compared to the corresponding non-relativistic system [7] in the case of a zero cosmological constant for both equal and unequal masses [8, 9]. The degrees of freedom in both the non-relativistic and relativistic systems can be rewritten in terms of a single particle moving in a two dimensional potential well of hexagonal symmetry. In the non-relativistic case the potential grows linearly as a function of radial distance, but in the relativistic case the growth is non-linear, yielding a potential in the shape of a hexagonal carafe. For both systems, two broad categories of periodic and quasi-periodic motion were found, referred to as annulus and pretzel orbits, as well as a set of chaotic motions appearing in the phase space between these two types. The phase space between the two systems was found to be qualitatively the same despite the

high degree of nonlinearity in the relativistic system.

In this paper we study the 3-body ROGS with non-zero cosmological constant Λ . This situation has no non-relativistic analogue. The effect of the cosmological constant is to induce a competing expansion/contraction of spacetime that competes with the gravitational self-attraction of the bodies. This system has been studied in some detail in the case of two interacting bodies, and it has been shown that relativistic effects are considerably enhanced by the presence of Λ [10]. For example a sufficiently large and positive Λ can overcome the attraction of the bodies, which then "lose casual" contact over a finite amount of proper time. The effect of Λ on the chaotic behaviour of the 3-body system has never been studied. It is the purpose of this paper to examine this problem, restricting our investigation to the equal-mass case.

In Sec. II we review the formalism of the N-body problem in lineal gravity. We discuss the canonical decomposition of the action and find the Hamiltonian of the particles in terms of the dilaton field, which is determined by a set of constraint equations. We employ two different methods for solving the constraint equations, which allow us to solve the equations of motion for systems with both positive and negative values for the cosmological constant in Sec. III. In Sec. IV we define a coordinate system that allows us to describe the three particle system as a single particle on a plane, moving in a potential well with hexagonal symmetry. We describe the shape of this potential and its dependence on momentum and the cosmological constant. Here we also find upper and lower bounds on allowed values of the cosmological constant in a system with a given energy. Using these new coordinates, we describe our methods for numerically solving the system in Sec. V, and our methods of obtaining orbits, Poincaré maps, and graphs of the oscillation patterns of the three particles. In Sec. VI, we numerically solve the equations of motion in the equal mass case with different values for the cosmological constant. We find two broad categories of periodic and quasiperiodic motions that we refer to as annulus and pretzel patterns, as well as a set of chaotic orbits found in the region of phase space in between these two types of orbits. We also identify general changes to the system in the presence of both a positive and a negative cosmological constant. Finally, in Sec. VII we present various Poincaré maps and discuss how the global phase space is distorted in the presence of a non-zero cosmological constant. We find that a negative cosmological constant considerably reduces the amount of chaotic behaviour, whereas a positive cosmological constant considerably enhances it. In Sec. VIII we discuss the salient features of our solutions and make some conjectures regarding their general properties. We close the paper with some concluding remarks and directions for further work.

2 Canonical Reduction of the N-body Problem in Linear Gravity

As in previous work [7, 8, 9] we begin with the action integral for the gravitational field coupled with N point particles, which is

$$I = \int d^2x \left[\frac{1}{2\kappa} \sqrt{-g} \left\{ \Psi R + \frac{1}{2} g^{\mu\nu} \nabla_\mu \Psi \nabla_\nu \Psi + \Lambda \right\} - \sum_{a=1}^N m_a \int d\tau_a \left\{ -g_{\mu\nu}(x) \frac{dz_a^\mu}{d\tau_a} \frac{dz_a^\nu}{d\tau_a} \right\}^{\frac{1}{2}} \delta^2(x - z_a(\tau_a)) \right] \quad (1)$$

where $g_{\mu\nu}$ and g are the metric and its determinant, R is the Ricci scalar, τ_a is the proper time of the a -th particle, $\kappa = 8\pi G/c^4$ is the gravitational coupling, and with a scalar (dilaton) field Ψ . This action describes a generally covariant self-gravitating system (without collision terms, so that the bodies pass through each other), in which the scalar curvature is sourced by the point particles and the cosmological constant Λ . Variation of the action with respect to the metric, particle coordinates, and dilaton field yields the field equations

$$R - \Lambda = \kappa T_\mu^{P\mu} \quad (2)$$

$$\frac{d}{d\tau_a} \left\{ \frac{dz_a^\nu}{d\tau_a} \right\} + \Gamma_{\alpha\beta}^\nu(z_a) \frac{dz_a^\alpha}{d\tau_a} \frac{dz_a^\beta}{d\tau_a} = 0 \quad (3)$$

$$\frac{1}{2} \nabla_\mu \Psi \nabla_\nu \Psi - g_{\mu\nu} \left(\frac{1}{4} \nabla^\lambda \Psi \nabla_\lambda \Psi - \nabla^2 \Psi \right) - \nabla_\mu \nabla_\nu \Psi = \kappa T_{\mu\nu}^P + \frac{\Lambda}{2} g_{\mu\nu} \quad (4)$$

where the stress-energy due to the point masses is

$$T_{\mu\nu}^P = \sum_{a=1}^N m_a \int d\tau_a \frac{1}{\sqrt{-g}} g_{\mu\sigma} g_{\nu\rho} \frac{dz_a^\sigma}{d\tau_a} \frac{dz_a^\rho}{d\tau_a} \delta^2(x - z_a(\tau_a)) \quad (5)$$

and is conserved. We observe that (2) and (3) form a closed system of $N+1$ equations for which one can solve for the single metric degree of freedom and the N degrees of freedom of the point masses. The evolution of the dilaton field is governed by the evolution of the point masses via (4). The left-hand side of (4) is divergenceless (consistent with the conservation of $T_{\mu\nu}$), yielding only one independent equation to determine the single degree of freedom of the dilaton.

We make use of the decomposition $\sqrt{-g}R = -2\partial_0(\sqrt{\gamma}K) + 2\partial_1(\sqrt{\gamma}N^1K - \gamma^{-1}\partial_1N_0)$ where the extrinsic curvature $K = (2N_0\gamma)^{-1}(2\partial_1N_1 - \gamma^{-1}N_1\partial_1\gamma - \partial_0\gamma)$, and rewrite the action in the form

$$I = \int dx^2 \left\{ \sum_a p_a \dot{z}_a \delta(x - z_a(x^0)) + \pi \dot{\gamma} + \Pi \dot{\Psi} + N_0 R^0 + N_1 R^1 \right\} \quad (6)$$

where $\gamma = g_{11}$, $N_0 = (-g^{00})^{-\frac{1}{2}}$, $N_1 = g_{10}$, π and Π are conjugate momenta to γ and Ψ respectively. The quantities N_0 and N_1 are Lagrange multipliers that enforce the constraints $R^0 = 0 = R^1$, where

$$R^0 = -\kappa \sqrt{\gamma} \gamma \pi^2 + 2\kappa \sqrt{\gamma} \pi \Pi + \frac{(\Psi')^2}{4\kappa \sqrt{\gamma}} - \left(\frac{\Psi'}{\kappa \sqrt{\gamma}} \right)' + \frac{\Lambda}{2\kappa} \sqrt{\gamma} - \sum_a \sqrt{\frac{p_a^2}{\gamma} + m_a^2} \delta(x - z_a(x^0)) \quad (7)$$

$$R^1 = \frac{\gamma'}{\gamma}\pi - \frac{1}{\gamma}\Pi\Psi' + 2\pi' + \sum_a \frac{p_a}{\gamma}\delta(x - z_a(x^0)) \quad (8)$$

with the symbols $(\dot{})$ and $()'$ denoting ∂_0 and ∂_1 , respectively. This action leads to the following system of field equations:

$$\begin{aligned} & \dot{\pi} + N_0 \left\{ \frac{3\kappa}{2}\sqrt{\gamma}\pi^2 - \frac{\kappa}{\sqrt{\gamma}}\pi\Pi + \frac{1}{8\kappa\sqrt{\gamma}\gamma}(\Psi')^2 - \frac{\Lambda}{4\kappa\sqrt{\gamma}} - \sum_a \frac{p_a^2}{2\gamma^2\sqrt{\frac{p_a^2}{\gamma} + m_a^2}}\delta(x - z_a(t)) \right\} \\ & + N_1 \left\{ -\frac{1}{\gamma^2}\Pi\Psi' + \frac{\pi'}{\gamma} + \sum_a \frac{p_a}{\gamma^2}\delta(x - z_a(t)) \right\} + N_0' \frac{1}{2\kappa\sqrt{\gamma}\gamma}\Psi' + N_1' \frac{\pi}{\gamma} = 0 \end{aligned} \quad (9)$$

$$\dot{\gamma} - N_0(2\kappa\sqrt{\gamma}\gamma\pi - 2\kappa\sqrt{\gamma}\Pi) + N_1 \frac{\gamma'}{\gamma} - 2N_1' = 0 \quad (10)$$

$$R^0 = 0 \quad (11)$$

$$R^1 = 0 \quad (12)$$

$$\dot{\Pi} + \partial_1 \left(-\frac{1}{\gamma}N_1\Pi + \frac{1}{2\kappa\sqrt{\gamma}}N_0\Psi' + \frac{1}{\kappa\sqrt{\gamma}}N_0' \right) = 0 \quad (13)$$

$$\dot{\Psi} + N_0(2\kappa\sqrt{\gamma}\pi) - N_1 \left(\frac{1}{\gamma}\Psi' \right) = 0 \quad (14)$$

$$\dot{p}_a + \frac{\partial N_0}{\partial z_a} \sqrt{\frac{p_a^2}{\gamma} + m_a^2} - \frac{N_0}{2\sqrt{\frac{p_a^2}{\gamma} + m_a^2}} \frac{p_a^2}{\gamma^2} \frac{\partial \gamma}{\partial z_a} - \frac{\partial N_1}{\partial z_a} \frac{p_a}{\gamma} + N_1 \frac{p_a}{\gamma^2} \frac{\partial \gamma}{\partial z_a} = 0 \quad (15)$$

$$\dot{z}_a - N_0 \frac{\frac{p_a}{\gamma}}{\sqrt{\frac{p_a^2}{\gamma} + m_a^2}} + \frac{N_1}{\gamma} = 0 \quad (16)$$

We can solve the constraint equations (11) and (12) in terms of the quantities $(\Psi'/\sqrt{\gamma})'$ and π' , since they are the only linear terms present. The generator obtained from the end point variation can then be transformed to fix the coordinate conditions. We can consistently

choose the coordinate conditions $\gamma = 1$ and $\Pi = 0$ [11]. Eliminating the constraints, the action then reduces to

$$I = \int d^2x \left\{ \sum_a p_a \dot{z}_a \delta(x - z_a) - \mathcal{H} \right\} \quad (17)$$

where the reduced Hamiltonian is

$$H = \int dx \mathcal{H} = -\frac{1}{\kappa} \int dx \Delta \Psi \quad (18)$$

where $\Delta \equiv \partial^2 / \partial x^2$, and $\Psi = \Psi(x, z_a, p_a)$ and is understood to be determined from the constraint equations which are now

$$\Delta \Psi - \frac{(\Psi')^2}{4} + \kappa^2 \pi^2 - \frac{\Lambda}{2} + \kappa \sum_a \sqrt{p_a^2 + m_a^2} \delta(x - z_a) = 0 \quad (19)$$

$$2\Delta \chi + \sum_a p_a \delta(x - z_a) = 0 \quad (20)$$

where $\pi = \chi'$. The consistency of this canonical reduction can be demonstrated by showing that the canonical equations of motion derived from the reduced Hamiltonian (18) are identical with (15) and (16) [11].

3 Solving the Constraint Equations

We can solve these two equations exactly for $N = 3$ particles by solving the equations in the empty spaces between particles and then matching the fields at each of the particle positions, imposing the condition that the Hamiltonian remains finite as $x \rightarrow \infty$. After these constraints are applied we are left with an equation containing only one unknown.

We divide the space into four regions determined by the arbitrary particle positions chosen so that $z_1 < z_2 < z_3$. We label the four regions: $x < z_1$ ((1) region), $z_1 < x < z_2$, ((2) region), $z_2 < x < z_3$ ((3) region), and $z_3 < x$ ((4) region). In each of these regions the solution to (20) is simply

$$\chi = -\frac{1}{4} \sum_{a=1}^3 p_a |x - z_a| - \epsilon X x + \epsilon C_\chi \quad (21)$$

with X and C_χ being two integration constants. The factor ϵ ($\epsilon^2 = 1$) changes sign under time reversal; it has been introduced to explicitly manifest the property that χ also changes sign under time reversal. We find an easier expression for (19) by using the substitution

$$\Psi = -4 \log |\phi| \quad (22)$$

which gives us

$$\Delta \phi - \frac{1}{4} \phi \left\{ -\frac{\Lambda}{2} + \kappa^2 (\chi')^2 \right\} = \frac{\kappa}{4} \sum_{a=1}^3 \sqrt{p_a^2 + m_a^2} \phi(z_a) \delta(x - z_a) \quad (23)$$

In the four regions defined above equation (23) has the solution

$$\phi = \left\{ \begin{array}{l} A_1 e^{\frac{1}{2}K_1 x} + B_1 e^{-\frac{1}{2}K_1 x} \quad \text{in the (1) region} \\ A_2 e^{\frac{1}{2}K_2 x} + B_2 e^{-\frac{1}{2}K_2 x} \quad \text{in the (2) region} \\ A_3 e^{\frac{1}{2}K_3 x} + B_3 e^{-\frac{1}{2}K_3 x} \quad \text{in the (3) region} \\ A_4 e^{\frac{1}{2}K_4 x} + B_4 e^{-\frac{1}{2}K_4 x} \quad \text{in the (4) region} \end{array} \right\} \quad (24)$$

where the K_i are defined as

$$\left\{ \begin{array}{l} K_1 = \sqrt{\kappa^2 \left[X - \frac{\epsilon}{4}(p_1 + p_2 + p_3) \right]^2 - \frac{\Lambda}{2}} \\ K_2 = \sqrt{\kappa^2 \left[X - \frac{\epsilon}{4}(-p_1 + p_2 + p_3) \right]^2 - \frac{\Lambda}{2}} \\ K_3 = \sqrt{\kappa^2 \left[X + \frac{\epsilon}{4}(p_1 + p_2 - p_3) \right]^2 - \frac{\Lambda}{2}} \\ K_4 = \sqrt{\kappa^2 \left[X + \frac{\epsilon}{4}(p_1 + p_2 + p_3) \right]^2 - \frac{\Lambda}{2}} \end{array} \right\} \quad (25)$$

The matching conditions that must be satisfied require that ϕ is continuous and its derivatives are consistent with integration of eq. (23) across the location of each particle:

$$\begin{aligned} \phi_2(z_1^+) &= \phi_1(z_1^-) \\ \phi_3(z_2^+) &= \phi_2(z_2^-) \\ \phi_4(z_3^+) &= \phi_3(z_3^-) \\ \phi_2'(z_1^+) - \phi_1'(z_1^-) &= \frac{\kappa}{4} \sqrt{p_1^2 + m_1^2} \phi(z_1) \\ \phi_3'(z_2^+) - \phi_2'(z_2^-) &= \frac{\kappa}{4} \sqrt{p_2^2 + m_2^2} \phi(z_2) \\ \phi_4'(z_3^+) - \phi_3'(z_3^-) &= \frac{\kappa}{4} \sqrt{p_3^2 + m_3^2} \phi(z_3) \end{aligned} \quad (26)$$

where $\phi_a(z_\beta^+) = \lim_{x \rightarrow z_\beta, x > z_\beta} \phi_a(x)$.

This leaves us with six equations for ten unknowns (A 's, B 's, X , and C_χ). There is also the condition that the Hamiltonian remains finite, which can be done by requiring

$$\Psi^2 - 4\kappa^2 \chi^2 + 2\Lambda x^2 = C_\pm x \quad (27)$$

where C_\pm are constants to be determined [11, 12]. This gives

$$A_1 = B_4 = 0$$

and four other equations that contain C_\pm . This leaves us with ten equations for ten unknowns ($A_2, A_3, A_4, B_1, B_2, B_3, C_\chi, C_-, C_+, X$). At this point, one can do the integration explicitly. The Hamiltonian becomes

$$H = -\frac{1}{\kappa} \int dx \Delta \Psi = -\frac{1}{\kappa} \left[-\frac{4\phi'}{\phi} \right]_{-\infty}^{+\infty} = \frac{2(K_1 + K_4)}{\kappa}$$

Without loss of generality, we choose the centre of inertia frame $p_1 + p_2 + p_3 = 0$, which simplifies the Hamiltonian to

$$H = \frac{4}{\kappa} \sqrt{\kappa^2 X^2 - \frac{\Lambda}{2}} \quad (28)$$

The Hamiltonian can only depend upon the relative separation of the particles and their conjugate momenta. Furthermore, in the equal mass case, the system is symmetric under particle interchange. We introduce the following notation

$$z_{ij} \equiv (z_i - z_j) \quad (29)$$

$$s_{ij} \equiv \text{sgn}(z_{ij}) \quad (30)$$

$$R_{i\pm} \equiv \sqrt{\kappa^2 \left[X - \frac{\epsilon}{4} \left(\sum_{a=1}^3 p_a s_{ai} \pm p_i \right) \right]^2 - \frac{\Lambda}{2}} \quad (31)$$

$$M_{ij} \equiv \kappa \sqrt{p_i^2 + m_i^2} + 2s_{ij} (R_{i+} - R_{i-}) \quad (32)$$

$$L_i \equiv -\kappa \sqrt{p_i^2 + m_i^2} + 2(R_{i+} + R_{i-}) \quad (33)$$

$$L_i^* \equiv \left(- \sum_{j < k \neq i} s_{ij} s_{ik} \right) \kappa \sqrt{p_i^2 + m_i^2} + 2(R_{i+} + R_{i-}) \quad (34)$$

where these quantities are defined in such a way that they automatically take care of the crossings of particles via s_{ij} . Using them, the derivation of the full determining equation for the Hamiltonian is similar to that for the $\Lambda = 0$ case [8]; the result is

$$\begin{aligned} L_1 L_2 L_3 &= M_{12} M_{21} L_3^* e^{\frac{1}{4} s_{21} [(M_{12} + L_1) z_{31} - (M_{21} + L_2) z_{32}]} \\ &+ M_{23} M_{32} L_1^* e^{\frac{1}{4} s_{32} [(M_{23} + L_2) z_{12} - (M_{32} + L_3) z_{13}]} \\ &+ M_{31} M_{13} L_2^* e^{\frac{1}{4} s_{13} [(M_{31} + L_3) z_{23} - (M_{13} + L_1) z_{21}]} \end{aligned} \quad (35)$$

or more compactly

$$L_1 L_2 L_3 = \sum_{ijk} |\epsilon_{ijk}| M_{ij} M_{ji} L_k^* e^{\frac{1}{4} s_{ij} [(M_{ij} + L_i) z_{ki} - (M_{ji} + L_j) z_{kj}]} \quad (36)$$

where ϵ_{ijk} is the Levi-Civita tensor.

While technically correct, the determining equation (35) is not useful computationally insofar as some of its terms can become imaginary with a sufficiently large cosmological constant; this is a consequence of eq. (25). However we can rewrite the determining equation to circumvent this problem. Consider the case where $z_1 < z_2 < z_3$. Redefining the following terms

$$\begin{aligned} \hat{M}_i &= \kappa \sqrt{p_i^2 + m_i^2} \\ \hat{K}_j &= -2 \sqrt{\kappa^2 \left[X + \frac{\epsilon}{4} \left(\sum_{i=1}^3 \sigma_{ji} p_i \right) \right]^2 - \frac{\Lambda}{2}} \end{aligned} \quad (37)$$

where $\sigma_{ji} = -1$ when $j \leq i$ and $\sigma_{ji} = 1$ when $i < j$ we can get a new form for the determining equation

$$\begin{aligned}
& \left[\left((\hat{M}_1 + \hat{K}_1) (\hat{M}_3 + \hat{K}_4) \hat{M}_2 + (\hat{M}_1 + \hat{K}_1) \hat{K}_3^2 + (\hat{M}_3 + \hat{K}_4) \hat{K}_2^2 \right) \tanh \left(\frac{1}{4} \hat{K}_3 z_{32} \right) \tanh \left(\frac{1}{4} \hat{K}_2 z_{21} \right) \right. \\
& + \left((\hat{M}_1 + \hat{M}_2 + \hat{K}_1) (\hat{M}_3 + \hat{K}_4) + \hat{K}_3^2 \right) \hat{K}_2 \tanh \left(\frac{1}{4} \hat{K}_3 z_{32} \right) \\
& + \left((\hat{M}_1 + \hat{K}_1) (\hat{M}_2 + \hat{M}_3 + \hat{K}_4) + \hat{K}_2^2 \right) \hat{K}_3 \tanh \left(\frac{1}{4} \hat{K}_2 z_{21} \right) \\
& \left. + (\hat{M}_1 + \hat{M}_2 + \hat{M}_3 + \hat{K}_1 + \hat{K}_4) \hat{K}_2 \hat{K}_3 \right] \\
& = 0
\end{aligned} \tag{38}$$

When the center of momentum is set to zero only the terms \hat{K}_2 or \hat{K}_3 can be imaginary. Consequently (38) is either purely real, or purely imaginary (in which case the i can be factored out). Permutation of the particles results in the exact same determining equation with the indices appropriately switched.

The Hamiltonian H is only implicitly determined from (38). Fortunately we do not need its explicit form since we can implicitly take derivatives on both sides of the determining equation (38) with respect to the phase space variables and from there extract the canonical equations of motion. From (28) with $p_Z = \sum_{a=1}^3 p_a = 0$, we obtain

$$\frac{\partial H}{\partial x_k} = \frac{4}{\kappa} \left(\frac{\partial}{\partial x_k} \sqrt{\kappa^2 X^2 - \frac{\Lambda}{2}} \right) = \frac{4\kappa X}{\sqrt{\kappa^2 X^2 - \frac{\Lambda}{2}}} \frac{\partial X}{\partial x_k} \tag{39}$$

where x_k is any of the canonical variables. We then have the simple but tedious task of taking $\frac{\partial}{\partial x_k}$ of both sides of equation (38), collecting the derivatives of X , and then converting them to derivatives of H via (39). This yields the canonical equations of motion

$$\dot{z}_a = \frac{\partial H}{\partial p_a} \tag{40}$$

$$\dot{p}_a = -\frac{\partial H}{\partial z_a} \tag{41}$$

where the dot denotes a derivative with respect to the coordinate time. These equations of motion are straightforward to calculate but highly tedious and will not be included here. When calculating the equations of motion for the particles when they are not in the arrangement $z_1 < z_2 < z_3$ we temporarily change the labels of the particles so that they do satisfy this condition. This allows us to use the derivatives of (38) to calculate the equations of motion for each of the particles, after which the original particle labels are returned. This method works regardless of whether or not the particles are identical.

4 General Properties of the Equations of Motion

We can now numerically calculate the equations of motion for each of the three particles. This would give us six equations of motion when our physical system only has four effective

degrees of freedom: two relative separations and their two conjugate momenta. Introducing the new variables

$$\begin{aligned} z_2 - z_1 &= \sqrt{2}\rho \\ -(z_1 + z_2) + 2z_3 &= \sqrt{6}\lambda \\ z_1 + z_2 + z_3 &= Z \end{aligned} \quad (42)$$

and their conjugate momenta

$$\begin{aligned} p_\rho &= \frac{1}{\sqrt{2}}(p_2 - p_1) \\ p_\lambda &= \frac{1}{\sqrt{6}}(-(p_1 + p_2) + 2p_3) \\ p_Z &= \frac{1}{3}(p_1 + p_2 + p_3) \end{aligned} \quad (43)$$

which have been chosen to satisfy the canonical commutation relations $\{q_i, p_j\} = \delta_{ij}$. This choice of variables gives the Hamiltonian an explicit sixfold symmetry. We can set the conjugate variables Z and p_Z to arbitrary values since Z is irrelevant in our equations and we can fix the center of inertia by setting $p_Z = 0$ without loss of generality. Inverting these relations, we get

$$\begin{aligned} z_2 - z_1 &= \sqrt{2}\rho \\ z_3 - z_2 &= \frac{1}{\sqrt{2}}(\sqrt{3}\lambda - \rho) \\ z_3 - z_1 &= \frac{1}{\sqrt{2}}(\sqrt{3}\lambda + \rho) \end{aligned} \quad (44)$$

and

$$\begin{aligned} p_1 &= -\frac{1}{\sqrt{2}}p_\rho - \frac{1}{\sqrt{6}}p_\lambda \\ p_2 &= \frac{1}{\sqrt{2}}p_\rho - \frac{1}{\sqrt{6}}p_\lambda \\ p_3 &= \sqrt{\frac{2}{3}}p_\lambda \end{aligned} \quad (45)$$

This choice of variables allows us to write the determining equation in terms of only $\{\rho, \lambda, p_\rho, p_\lambda\}$ for a given cosmological constant. In this way, the relativistic Hamiltonian can be regarded as a function $H = H(\rho, \lambda, p_\rho, p_\lambda)$

We see from this perspective that the linear three-particle system is equivalent to a single particle moving in a two dimensional ‘‘potential well’’. This allows the variables $\rho, \lambda, p_\rho, p_\lambda$ to be interpreted as the coordinates and the conjugate momenta of this single particle, which we call the hex-particle due to the hexagonal symmetry of the potential. In the Newtonian case, the potential takes on the shape of a hexagonal-shaped cone with planar sides and is

independent of the momenta [13]. The relativistic potential well is obtained by regarding the potential to be the difference between the Hamiltonian and the relativistic kinetic energy

$$V(\rho, \lambda) |_{p_\rho=a, p_\lambda=b} = H(\rho, \lambda, p_\rho = a, p_\lambda = b) - \sqrt{(mc^2)^2 + (c|p|)^2} \quad (46)$$

and is dependent on the momentum $|p| = \sqrt{a^2 + b^2}$ of the hex-particle as well as its position in the (ρ, λ) plane⁴.

We get our first look at the relativistic potential by considering the case when $p_\rho = 0 = p_\lambda$:

$$V(\rho, \lambda) |_{p_\rho=0, p_\lambda=0} = H(\rho, \lambda, p_\rho = 0, p_\lambda = 0) - mc^2$$

At very low energies this relativistic potential is indistinguishable from the potential for the Newtonian case. However, as shown in table (1), even at energies only moderately larger than the rest mass, the sides of the hexagon become convex in the relativistic potential. Though it retains its hexagonal symmetry, the growth of the relativistic potential is very rapid as ρ and λ increase. The size of the cross section of the potential reaches a maximum at an energy V_{Rc} just over twice the rest energy of the particle, after which the diameter of the potential decreases like $\ln(V_R)/V_R$ with increasing V_R [8].

The part of the potential on the branch with $V_R > V_{Rc}$ is in an intrinsically nonperturbative relativistic regime. The motion for values of V_R larger than this cannot be understood as a perturbation from some classical limit of the motion. The nonrelativistic hexagonal cone becomes a hexagonal carafe in the relativistic case, with a neck that narrows as V_R increases.

When $p_\rho = 0 = p_\lambda$ it is straightforward to show that the potential is independent of the cosmological constant, a feature noted previously in the 2-body system [10, 12]. However, for nonzero p this is not the case, and we map out the potential to show how it changes as Λ varies. It is convenient to instead map the potential with set values of radial momentum p_r and angular momentum p_θ of the hex-particle where

$$p_r = p_\rho \cos \theta + p_\lambda \sin \theta$$

$$p_\theta = -p_\rho \sin \theta + p_\lambda \cos \theta$$

$$\theta = \arctan\left(\frac{\lambda}{\rho}\right)$$

since the change to polar coordinates manifestly retains the hexagonal symmetry of the potential, which greatly simplifies the subsequent analysis.

First, when $\Lambda = 0$ and the hex particle has positive radial momentum p_r , the width of the potential at lower energies increases with increasing p_r and the sides of the hexagonal

⁴Note that earlier definitions of the potential [8] defined it to be the value of the Hamiltonian at zero momenta.

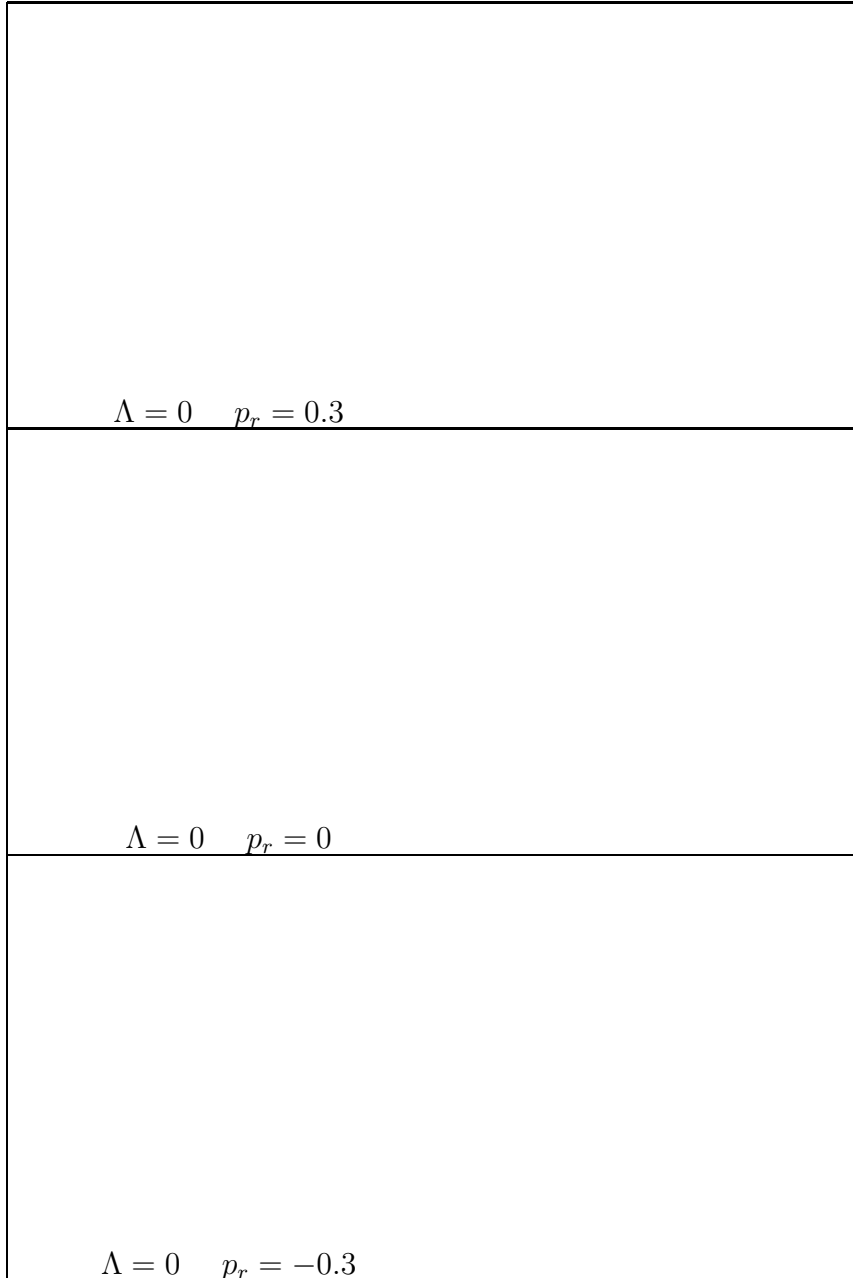


Table 1: Potential plot for $\Lambda = 0$ from both side and top views with solid lines denoting equipotentials.

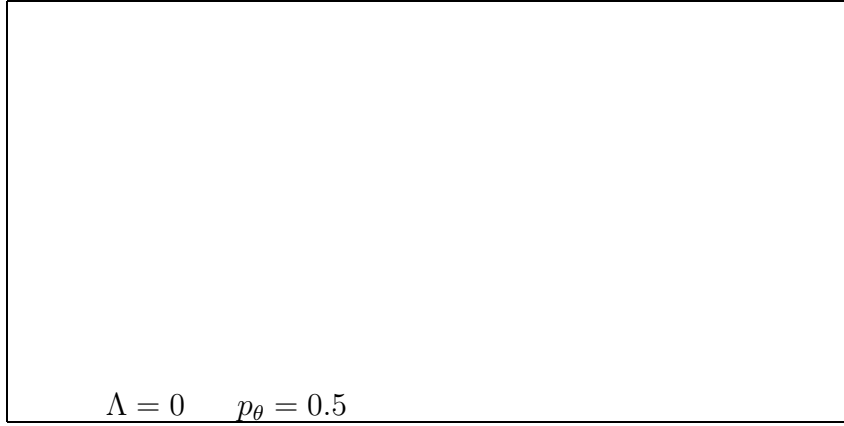


Table 2: Potential plot with positive angular momentum from both side and top views with solid lines denoting equipotentials.

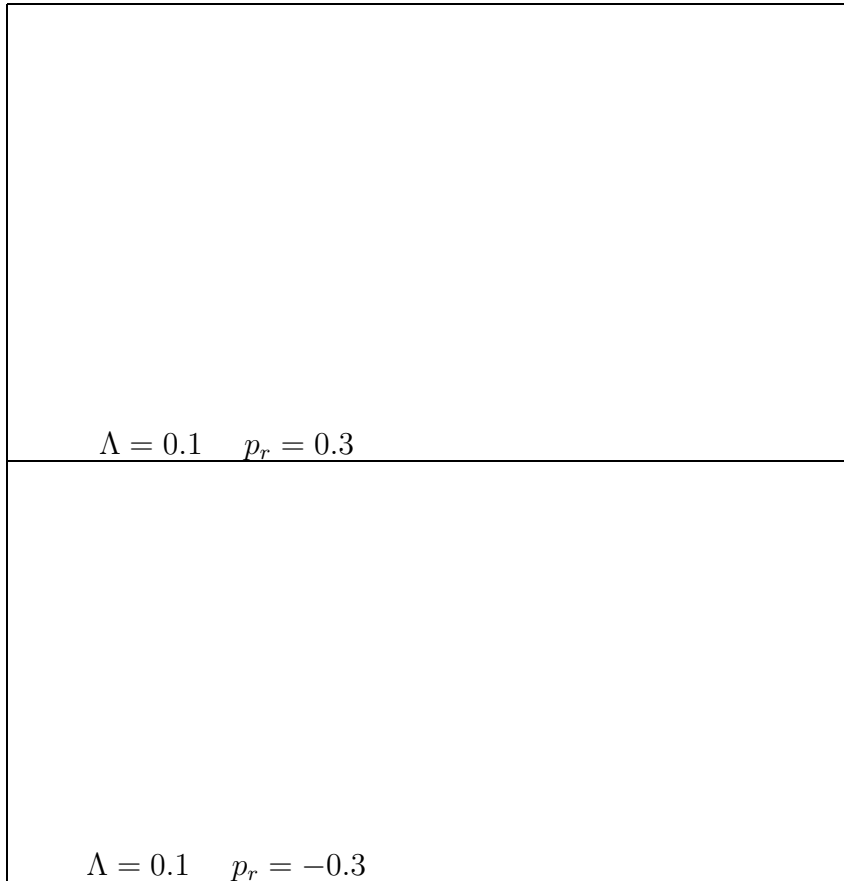


Table 3: Potential plots for $\Lambda > 0$ from both side and top views with solid lines denoting equipotentials.

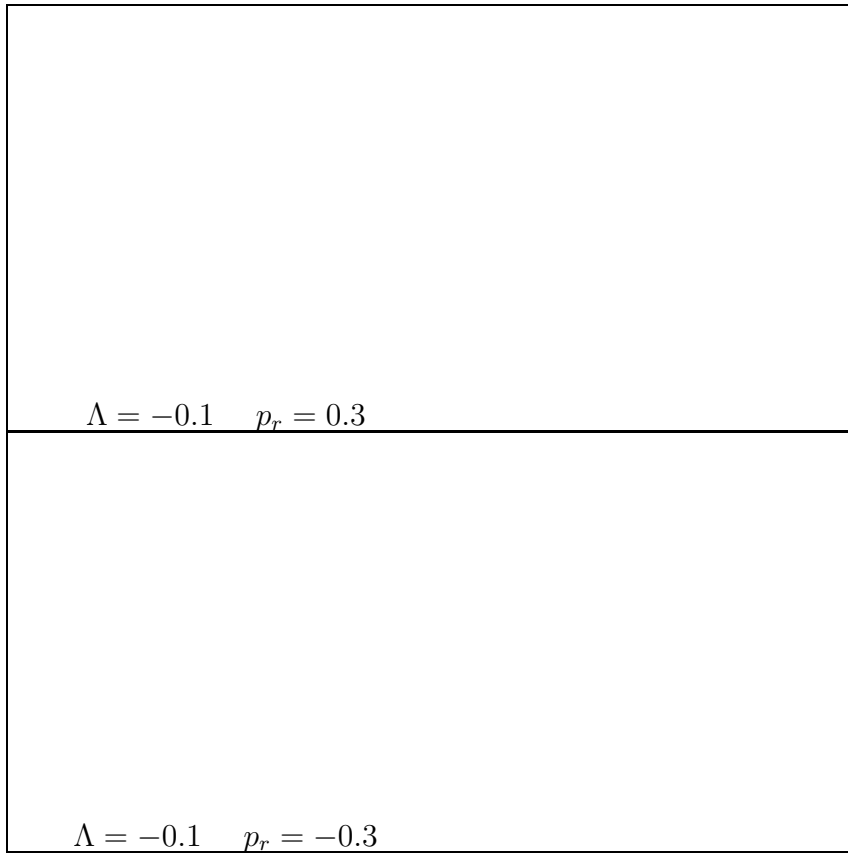


Table 4: Potential plots for $\Lambda < 0$ from both side and top views with solid lines denoting equipotentials.

cross section become more convex at lower energies, resulting in a star shaped cross section, as shown in table (1). This widens the bottom of the potential, and lowers the value of V_{Rc} at which the cross-section of V is at its largest. When the hex-particle has negative p_r the opposite happens: the width of the potential decreases and the sides of the hexagonal cross section become more concave, resulting in a more rounded cross section. Though its sides are initially much steeper, the potential curves back in on itself much more gradually resulting in a higher value of V_{Rc} .

A similar analysis for nonzero angular momentum p_θ , as shown in table (2), indicates that only for very high values does it have any substantive effect on the potential. As p_θ increases the sides of the hexagonal cross section become concave and slightly skewed in the direction opposing the angular momentum. We expect that this is the cause of the previously observed rotation of the annulus orbits at higher energies [8] for the $\Lambda = 0$ case.

When $\Lambda > 0$ the potential, shown in table (3), shifts down slightly when p_r is positive. At lower energies the sides are pushed farther out while becoming more convex in a manner similar to that which occurs for positive radial momentum in the original ($\Lambda = 0$) potential. A side effect of this is that it seems to lower V_{Rc} , which may cause the system to become unstable at lower energies. Associated with this is the appearance of a positive critical value of the cosmological constant, which we will discuss in more detail later. For negative p_r and $\Lambda > 0$, at lower energies the potential is pulled inward and becomes more concave, again in a manner similar to the negative radial momentum in the $\Lambda = 0$ case. However, the magnitude of this effect of Λ on $p_r < 0$ is much less than the effect on $p_r > 0$. The effects noted above for angular momentum also seem to increase when $\Lambda > 0$. Overall, the presence of a positive cosmological constant seems to enhance the effects that momentum has on the $\Lambda = 0$ potential.

When $\Lambda < 0$, as shown in table (4), the opposite effect happens. For $p_r > 0$ the sides are pulled in relative to the effects of momentum in the $\Lambda = 0$ potential, reducing its diameter as well as making the sides less convex. For $p_r < 0$, the sides of the potential are very slightly pushed back out relative to the effects of momentum in the $\Lambda = 0$ potential, increasing its diameter. The effects of angular momentum are also counteracted when $\Lambda < 0$, so overall, the presence of a negative cosmological constant seems to reduce momentum-dependence in the potential.

We have found both upper and lower limits on the range of allowed values of the cosmological constant Λ that are dependent on the energy in the system. As described before, in order to solve the equations of motion we must calculate the derivatives of X from Eq. (21) with respect to each z_i and p_i , and then use Eqs. (28) and (39) to convert X -derivatives to H -derivatives, yielding the canonical equations of motion. However, both X and H must be real. Thus from eq. (28) we find that for any given value of H , Λ must be chosen in a range that satisfies

$$H \geq \frac{4}{\kappa} \sqrt{-\frac{\Lambda}{2}}$$

resulting in a negative critical value for Λ

$$\Lambda_{negcrit} = -\frac{H^2 \kappa^2}{8} \tag{47}$$

As $\Lambda \rightarrow \Lambda_{negcrit}^+$, we see that $X \rightarrow 0$. From eq. (39) all of the derivatives of H tend to

zero, rendering the particle motionless. If we take a fixed value for H_0 and increase it by an arbitrarily small amount h , when Λ is the negative critical value for an energy of H_0 , from eqs. (28, 47) we get

$$H = H_0 + h = \frac{4}{\kappa} \sqrt{\kappa^2 X^2 + \frac{\Lambda_{negcrit}}{2}} = H_0 \sqrt{1 + \frac{16X^2}{H_0^2}}$$

When h is very small, so is X , and we can take the approximation $h \simeq 8 \frac{X^2}{H_0}$, yielding

$$\frac{\partial H}{\partial x_n} = \frac{\partial h}{\partial x_n} = \frac{16X}{H_0} \frac{\partial X}{\partial x_n} = \sqrt{\frac{32h}{H_0}} \frac{\partial X}{\partial x_n} \quad (48)$$

for the equations of motion, where x_n is any of the canonical variables. For small h the equations of motion are all scaled by \sqrt{h} , which is equivalent to scaling the time factor by $\frac{1}{\sqrt{h}}$. Consequently, when the cosmological constant is very close to its negative critical value for a system with a given energy, the hex-particle will not so much be restricted in its movement in the (ρ, λ) plane, and follow that orbit at a much slower pace. However, as we will describe in more detail later, we have found that for small negative values for the cosmological constant the frequency of the hex-particle's movement increases, so this trend only appears for very small h .

We have not been able to identify analytically the positive critical value of Λ . Rather we identify it numerically: when running simulations with Λ too large the three particle system breaks out of its bound state, and our simulation breaks down. We have not yet been able to conclusively find why the system fails where it does, but we believe it may be due to the fact that, when radial momentum is present in the hex-particle system, a positive cosmological constant seems to lower the value of V_{Rc} , rendering the system intrinsically nonperturbative where it was previously in a perturbative regime. This hypothesis is supported by the fact that, for the energies that we have tested, the maximum value of Λ allowed seems to decrease substantially as H increases.

The effect on the hex-particle's orbits from approaching these positive and negative critical values of the cosmological constant will be further discussed in later sections.

5 Methods for Solving the Equations of Motion

We find it easier to study the equal mass three body system by analyzing the motion of the hex-particle in the (ρ, λ) plane. In this system the bisectors joining opposite vertices of the potential well correspond to two of the three particles crossing one another, causing a discontinuous change in the hex-particle's acceleration. Therefore, in the Hamiltonian formalism, the motion of the hex-particle is governed by a pair of differential equations which are continuous everywhere except at the three hexagonal bisectors $\rho = 0$, $\rho - \sqrt{3}\lambda = 0$, and $\rho + \sqrt{3}\lambda = 0$. These correspond to the crossings of particles 1 and 2, 2 and 3, or 1 and 3 respectively.

We allow the hex-particle to freely cross over each of these bisectors, which corresponds to a pair of particles passing through each other. An analogous system in the Newtonian

case, consists of the motions of a ball under a constant gravitational force elastically colliding with a wedge [14]. This system is nearly identical to the one we study insofar as, in the equal mass case, an elastic collision between a pair of particles in the three body system cannot be distinguished from a crossing of two equal mass particles. However, a distinction between the two systems in a certain class of orbits has been previously observed [8].

The nonsmoothness of the potential gives rise to interesting dynamics in the system. We shall refer to two distinct types of motion in our subsequent analysis [14]. A motion, corresponding to the same pair of particles crossing twice in a row in the three body system (or equivalently the hex-particle crossing a single bisector twice in succession), and *B* motion, in which a single particle crosses both of the other particles in succession (or equivalently the hex-particle crossing two successive hexagonal bisectors). For a given orbit we can characterize the motion by a sequence of these symbols with a finite exponent n denoting n repeats and an overbar denoting an infinite repeated sequence. It is important to note that the classification of a crossing as *A* or *B* motion is dependent on the previous crossing, so there is an ambiguity in the classification of either the final or the initial crossing. This is resolved by taking the initial crossing as unlabeled; since we are considering large sequences of motion this ambiguity causes no practical difficulties [8].

There is a technical difficulty in comparing trajectories in systems with different values for the cosmological constant. Such changes induce a change in the determining equation and so we cannot use exactly the same initial conditions. We will deal with this by comparing trajectories with the same fixed-energy (FE) initial conditions. This is done by fixing the initial values of H , ρ , λ and p_ρ , and adjusting p_λ so that the Hamiltonian constraint is satisfied.

We have implemented three methods of analysis to study the motion of the system. First, we plot the trajectory of the hex-particle in the (ρ, λ) plane and compare the motion under different initial conditions and in systems with a different value for the cosmological constant. Second, we plot the motion of the three particles as a function of time which gives us a different method for visualization, allowing us to identify differences in the various types of motion. Third, we construct Poincare sections by plotting the radial momentum (p_r , labeled as x) against the square of the angular momentum (p_θ^2 , labeled as z) of the hex-particle each time it crosses one of the bisectors. When all particles have equal mass, all of the bisectors are equivalent so all of the crossings can be plotted on the same surface of section. This allows us to easily identify regions of periodicity, quasiperiodicity, and chaos, and we will discuss each of these features.

There is no closed-form solution for either the determining equation (35) or to the equations of motion so we must solve these equations numerically. We proceed by introducing dimensionless variables

$$X = M_{tot}\hat{x} \quad H = M_{tot}\hat{h} \quad \Lambda = M_{tot}\kappa\hat{\Lambda}$$

where $M_{tot} = \sum_{a=1}^3 m_a$, and also

$$p_i = M_{tot}\hat{p}_i \quad z_i = \frac{4}{\kappa M_{tot}}\hat{z}_i$$

Substituting these variables into Eqs. (31), (32), (33), (34) we get

$$R_{i\pm} = \kappa M_{tot} \sqrt{\left[\hat{x} - \frac{\epsilon}{4} \left(\sum_{a=1}^3 \hat{p}_a s_{ai} \pm \hat{p}_i \right) \right]^2 - \frac{\hat{\Lambda}}{2}} \equiv \kappa M_{tot} \hat{R}_{i\pm}$$

$$\sqrt{p_a^2 + m_a^2} = M_{tot} \sqrt{\hat{p}_a^2 + \hat{m}_a^2}$$

which gives us

$$M_{ij} \equiv \kappa M_{tot} \hat{M}_{ij} \quad L_i \equiv \kappa M_{tot} \hat{L}_i \quad L_i^* \equiv \kappa M_{tot} \hat{L}_i^*$$

The notation for these new variables have exactly the same form but without the factor of kappa inside the square roots and all multiplied by a factor of κM_{tot} . Thus when writing the determining equation in dimensionless variables the factors of $(\kappa M_{tot})^3$ cancel out everywhere and the exponential factors become

$$s_{ji} \left[\kappa M_{tot} (\hat{M}_{ij} + \hat{L}_i) \frac{1}{\kappa M_{tot}} \hat{z}_{ki} - \kappa M_{tot} (\hat{M}_{ji} + \hat{L}_j) \frac{1}{\kappa M_{tot}} \hat{z}_{kj} \right] = s_{ji} \left[(\hat{M}_{ij} + \hat{L}_i) \hat{z}_{ki} - (\hat{M}_{ji} + \hat{L}_j) \hat{z}_{kj} \right]$$

So we see that introducing dimensionless variables is equivalent to writing the determining equation with κM_{tot} set equal to unity.

We numerically integrate the equations of motion generated from the determining equation (38) using a MatLab ODE routine (ODE45 or ODE113). When the particles are not in the arrangement $z_1 < z_2 < z_3$ our program temporarily changes the labels on the particles so they satisfy this condition. The equations of motion are then calculated for each of the particles and their original labels are returned. This method works regardless of whether or not the particles are identical.

For the Poincare sections we stopped the integration each time the hex-particle crossed one of the bisectors by using an “events” function and saving the values of radial and angular momentum for plotting. Ideally for each chaotic trajectory the Poincare section should be allowed to run for a long time in order to accurately determine which regions of the plane the chaotic motion extended to and which regions were restricted.

In order to control errors, we imposed absolute and relative error tolerances of 10^{-8} for the numerical ODE solvers. For the values of H we studied this yielded numerically stable solutions. We tested this by checking that the energy in the system remained constant throughout the motion to a value no larger than 10^{-6} .

6 Equal Mass Trajectories

We look at the cases where all three particles have equal mass and the hexagonal symmetry of the potential well is maintained. As described in previous papers [8] we find three general classes of orbits which we denote as annuli, pretzel, and chaotic. Examples of these classes of orbits have been found at all energies and in the presence of a positive and negative cosmological constant.

Furthermore, in each class there are orbits that eventually densely cover the region of the (ρ, λ) space that they occupy and orbits that do not. The latter situation corresponds

Figure 1: Examples of near-periodic orbits (run for 200 time units), trajectories do not cover the entire (ρ, λ) space. Periodic annulus and pretzel orbits can be found for almost all testable energies and values of Λ .

to a regular orbit that repeats itself after a finite time – the symbol sequence consists of a finite sequence repeated infinitely many times, resulting in a periodic trajectory. The former situation corresponds to an orbit where the same finite sequence is repeated, but with A motion added or removed at irregular intervals, resulting in a quasiperiodic trajectory.

The quasiperiodic orbits closely resemble the periodic orbits, except that they fail to exactly repeat themselves and have some form of precession that causes the orbits to fill a region of space. Thus these quasiperiodic orbits show a high degree of regularity, manifest by its periodic symbol sequence.

6.1 Annulus Orbits

The annuli are orbits where the hex-particle never crosses the same bisector twice in succession, resulting in the symbol sequence \overline{B} and an orbit in the shape of an annulus encircling the origin in the (ρ, λ) plane.

These annulus orbits can be both quasiperiodic and fill in the entire ring, while a few repeat themselves after some number of rotations about the origin. Since periodic orbits are very difficult to find numerically, the orbits in the figures are actually just very close to being periodic, so that the pattern of the periodic orbit can be seen.

There is a slight rotation in the annulus orbits as H increases, but otherwise little qualitative difference between the annulus orbits occurs for different energies. However we do see some qualitative changes to the orbits as Λ changes. For the larger positive values of Λ that

Figure 2: Arbitrary examples of quasi-periodic orbits that densely fill the (ρ, λ) space (run for 200 time steps). Quasi-periodic annulus and pretzel orbits can be found at all testable energies and values of Λ .

Figure 3: Annulus orbits for zero cosmological constant ($H = 1.2$ lower left; $H = 1.8$ upper right) shown in conjunction with their corresponding three-particle trajectories. The vertical axis is the displacement from the origin in units of $\kappa M_{tot} c^2/4$. These orbits have been run for 200 time steps but the three-particle trajectory plots have been truncated after 30 time steps. The rotation in the annulus orbits is greater for the higher energy example.

Figure 4: Overlay of annulus orbits at $H = 1.5$ starting with the same FE initial conditions but with different values for Λ run for 200 time steps and their corresponding three-particle trajectories truncated after 30 time steps (top $\Lambda = 0.02$; middle $\Lambda = 0$; bottom $\Lambda = -0.25$).

we can obtain numerically, we find for the same FE initial conditions that the outer part of the annulus extends farther out into the (ρ, λ) plane. We also find that the width of the annulus also increases more than if the orbit were simply linearly dilated (ie ‘photographically enlarged’). Conversely, for large negative Λ the orbit covers less of the (ρ, λ) plane and the annulus becomes thinner by a greater factor. These effects can be seen in figure (4) and seem to be consistent with how the potential changes with Λ . For positive Λ , the effect that positive radial momentum has on pushing out the potential and negative radial momentum on pulling the potential in towards the origin is exaggerated. Hence when the hex-particle is moving radially outward it will go farther because the potential is being pushed back. Similarly when the hex-particle is moving radially inward it will go farther because the potential is being pulled in and driving it farther. For negative Λ the opposite occurs and the radial motion is somewhat damped, resulting in a smaller range of radial motion.

Another characteristic change induced by Λ is that the frequency of the three particle motion decreases as Λ becomes positive and increases as Λ becomes negative. At values of Λ extremely close to the negative critical value given in Eq. (47) the frequency of the motion should eventually decrease as described in Eq. (48). However, our simulation breaks down due to error tolerance limits so at this time we have not been able to verify this property numerically. This non-linear change in frequency can result in the same set of

Figure 5: Examples of pretzel orbits for $\Lambda = 0$ ($H = 1.8$, lower left; $H = 1.5$, upper right) run for 200 time steps and shown in conjunction with their corresponding three-particle trajectories truncated after 60 time steps. Interactions resembling a quasistable bound subsystem of two particles orbiting a third particle can clearly be seen.

initial conditions producing periodic or quasiperiodic orbits depending on Λ . This change in frequency has been observed in all three types of orbits.

6.2 Pretzel Orbits

In Pretzel orbits, the hex-particle essentially oscillates back and forth about one of the bisectors, corresponding to a stable or quasistable bound subsystem of two particles. This bound pair then orbits the remaining particle, which corresponds to the hex-particle oscillating along the same bisector. The existence of a two-particle bound subsystem was discovered in the Newtonian case [15] and has been observed previously in the $\Lambda = 0$ case [8]. Symbolically, these orbits can be written as $\prod_{ijk} (A^{n_i} B^{3m_j})^{l_k}$, where $n_i, m_j, l_k \in Z^+$, with some l_k possibly infinite. This motion results in an extremely diverse collection of orbits. Many families of regular orbits exist, containing one base element (for example AB^3) and a sequence of elements formed by appending an A to each existing sequence of A's (for example $\{AB^3, A^2B^3, A^3B^3, \dots\}$). This results in an extremely complex structure for the phase space, which we will analyze later.

Figure 6: Overlay of pretzel orbits starting with the same FE initial conditions but with different values for Λ run for 200 time steps and their corresponding three-particle trajectories truncated after 30 time steps (top $\Lambda = 0.02$; middle $\Lambda = 0$; bottom $\Lambda = -0.25$).

The B^3 term in the above sequences corresponds to a 180° swing of the hex-particle around the origin, and the orbits in the (ρ, λ) plane that result from this motion comprise a wide variety of twisted, pretzel-like figures. Again, in this class of orbits we find both periodic orbits with an infinitely repeating symbol sequence, and quasiperiodic orbits that densely fill a cylindrical tube in the (ρ, λ) plane which usually has a kink about the $\lambda = 0$ line.

Qualitatively, the characteristics of the pretzel orbits are very similar at different energies. At all of the values of H that we can obtain numerically we can find orbits of all of the different allowed families that have regular symbol sequences. One of the differences is that it seems that the kinks in at the $\lambda = 0$ line become more pronounced at higher energies, as previously observed in [8].

As we change the cosmological constant we see many similar changes to the pretzel orbits that we found for the annulus orbits. As Λ increases the orbits extend farther out on the (ρ, λ) plane, corresponding to the widening of the potential with positive radial momentum described before. Alternatively, as Λ decreases the orbits cover less of the (ρ, λ) plane, corresponding to the contracting of the potential with negative radial momentum. We can find orbits with the same regularly repeating symbol sequence for all values of Λ that we can obtain numerically. However, as Λ becomes positive we have found that some pretzel orbits

begin to show a form of chaotic behaviour not seen in the $\Lambda \leq 0$ cases. We will describe these cases in more detail later.

Again in the three body figures we find that the frequency of the motion is increased and reduced for negative and positive Λ respectively. This non-linear change in frequency can cause the same set of initial conditions to result in either periodic or quasiperiodic motion depending on Λ . However in addition to this we find that the orbit shape and symbol sequence can be drastically changed as well. We will be able to see the overall structure of the change when we begin to look at the bottom region of the Poincaré maps.

6.3 Chaotic Orbits

The chaotic orbits are those in which the hex-particle wanders between A motion and B motion in a seemingly irregular fashion. On the Poincaré section these orbits appear as densely filled regions. These orbits eventually wander into all areas of the (ρ, λ) plane allowed by the energy constraint, a trait not seen in either the annuli or pretzel orbits. Areas of chaos can be found in this system at the transition point between annulus and pretzel orbits, though the size of the chaotic region seems to be highly dependent on the cosmological constant, as will be shown later.

Chaotic orbits have been found at all values of H that are numerically obtainable and have essentially the same basic properties. However these orbits are generally hard to find at any energy as they are very sensitive to initial conditions. The top left orbit of figure 7 gives us an example of a chaotic orbit found in between the annulus and pretzel regions on the Poincaré section. We can see that the orbit sometimes shows the characteristic motion of an annulus orbit and sometimes shows the motion of a pretzel orbit. The three-particle trajectories show us how the particles switch roles during their quasi-regular motion at irregular intervals resulting in the chaotic motion.

As with the annulus and pretzel orbits, the chaotic orbits extend farther out into the (ρ, λ) plane as Λ increases, and the frequency of the three particle motion increases. However, chaotic orbits are non-periodic by definition, so a change in frequency can never make this type of orbit periodic.

The most significant change to the chaotic orbits at different values of Λ is that as Λ becomes negative, the initial conditions that resulted in a chaotic orbit will generally result in either an annulus or pretzel orbit. Conversely, we have found more initial conditions resulting in chaotic orbits when Λ is positive. Overall there seems to be a strong positive correlation between the value of the cosmological constant and the size of the subset of initial conditions that result in chaotic orbits. This trend is illustrated by figure (8) where for the same FE initial conditions are run with different values of Λ . The initial condition that results in chaotic orbits for $\Lambda \geq 0$ instead result in a regular annulus orbit (in this case) for $\Lambda < 0$.

In addition, we have also found separate regions of chaos within the pretzel region of the Poincaré map when Λ is positive. For certain initial conditions resulting in pretzel orbits when $\Lambda = 0$, when we increase Λ we find that the hex-particle begins to irregularly transverse increasingly larger regions of the (ρ, λ) plane. However, these chaotic pretzel orbits do not cover the entire (ρ, λ) plane as do the chaotic orbits in between the annulus and pretzel regions. An example of this type of orbit is shown on the bottom left of figure (7). In these

Figure 7: Examples of chaotic orbits run for 200 time steps between the pretzel and annulus regions (top right) and within the pretzel region (bottom left) along with their corresponding three-particle trajectories truncated after 60 time steps. The sizes of the regions of chaos are highly dependent on the cosmological constant and the chaotic orbits in the pretzel regions are only found when $\Lambda > 0$.

Figure 8: Chaotic orbits for $H = 1.2$ starting with the same FE initial conditions but with different values for Λ run for 200 time steps (top left $\Lambda = 0.06$; top right $\Lambda = 0$; bottom $\Lambda = -0.175$). Not overlapped to emphasize change in amount of chaotic motion

chaotic pretzel orbits – unlike the previously described chaotic orbits where all three particles switch positions at irregular intervals – we can see from the three-particle motion that while two of the particles orbit each other closely in a bound subsystem, the third particle shows fairly regular motion. The chaotic motion of the hex-particle results from irregular motions in the two-particle subsystem.

7 Poincaré Plots

We now consider the Poincaré sections for this system. These are constructed by plotting the square of the angular momentum (p_θ^2 , labeled as z) of the hex-particle against its radial momentum (p_r , labeled as x) each time it crosses one of the bisectors. Since we are looking only at the case when all three particles have the same mass, all of the bisectors are equivalent, and so we can plot all of the crossings on the same surface of section. This allows us to find regions of periodicity, quasiperiodicity, and chaos.

Since this system is governed by a time-independent Hamiltonian with four degrees of freedom, the total energy is a constant of the motion and the phase space is a three-dimensional hypersurface in four dimensions. If an additional constant of motion exists the system is said to be integrable, and its trajectories are restricted to two-dimensional surfaces in the available phase space. Since the trajectories can never intersect, that constraint imposes severe limitations on the types of motion that integrable systems can exhibit. Trajectories may be periodic (repeating themselves after a finite interval of time) or quasiperiodic. Since the trajectories are, by definition, comprised by the intersection of two two-dimensional surfaces, they will always appear as lines or dots for quasiperiodic and periodic orbits respectively, on the Poincaré section. This is a sharp contrast to the case when all orbits can move freely in three dimensions in a completely nonintegrable system. The extra degree of freedom permits an orbit to visit all regions of phase space, and the system typically displays strongly chaotic behaviour. Such trajectories appear as filled-in areas on the Poincaré map.

When an integrable system is given a sufficiently small perturbation, most of its orbits remain confined to two-dimensional surfaces. However, it is possible that small areas of chaos will appear sandwiched between the remaining two-dimensional surfaces, which can grow as the magnitude of the perturbation is increased, eventually becoming connected areas on the Poincaré section. This phenomenon is called a Kolmogorov-Arnold-Moser (KAM) transition [16]. Within these regions, islands of regularity may remain for quite some time and can have an intricate fractal structure [17], but the system will typically become almost fully ergodic for sufficiently large perturbations [18].

The outer bound of the Poincaré section is limited by the energy of the system. The first noticeable feature is that it is not symmetric about the $p_r = 0$ axis, but is instead skewed to the right, with the deformation increasing with H . This is at first puzzling; the trajectories of a subset of the annulus orbits always have positive radial velocities when they intersect one of the hexagon's edges and the tendency of all annulus orbits is to have $p_r > 0$ at the bisectors. However, it occurs because the Hamiltonian given by (35) and (38) is not invariant under the discrete symmetry $p_i \rightarrow -p_i$, but is only invariant under the weaker discrete symmetry $(p_i, \epsilon) \rightarrow (-p_i, -\epsilon)$. The parameter $\epsilon = \pm 1$ is a discrete constant of integration that is a measure of the flow of time of the gravitational field relative to the

Figure 9: The Poincaré plot of the system at $H = 1.2$ and $\Lambda = 0$. The upper inset shows a close up of the upper chaotic region where the Poincaré plot is filled in. The lower inset shows a close up of the structure in the pretzel region.

Figure 10: The Poincaré plot for $H = 1.2$ and $\Lambda = -0.175$, just above the critical value of -0.18 for that energy. The upper inset gives a close up of the very tiny remaining region of chaos. The lower inset gives a close up of the structure of the lower right pretzel region.

Figure 11: The Poincaré plot for $H = 1.2$ and $\Lambda = 0.06$, near the highest value we can obtain numerically. The upper and lower insets provide successive closeups of the lower right pretzel region showing both the regions of pretzel chaos and the self-similar structure at increasingly small scales.

particle momenta. In our study we have chosen $\epsilon = +1$ throughout, which has the effect of making the principal features of the Poincaré plot “squashed” towards the lower right-hand side of the figure. If we had chosen $\epsilon = -1$ this deformation would be towards the lower left side. This is reminiscent of the situation for two particles, in which the gravitational coupling to the kinetic energy of the particles causes a distortion of the trajectory from an otherwise symmetric pattern [19, 20] becoming more pronounced as H increases.

The general structure of the Poincaré section can be seen in figure (9). There is a fixed point just right of the center of the plot surrounded by triangular rings. These near-integrable curves correspond to the annulus orbits for that energy. All of the possible annulus orbits are contained in the largest triangular ring surrounding this region. Its boundary contains a thin region of chaos and outside of that, at the bottom and top corners, we have the regions corresponding to the pretzel orbits.

The structures in the lower part and upper corners of the Poincaré section is extremely complicated. We find a self similarity in these regions with a series of circles bounding the quasiperiodic near-integrable regions repeating themselves on increasingly smaller scales. We find that each of these circular patterns corresponds to a family of pretzel orbits. The two largest circles just below the annulus region correspond to the boomerang-shaped orbits ($\overline{AB^3}$). The next set of three circles corresponds to the sequence ($\overline{A^2B^3}$), and so on. We see a collection of crescents between these sets of circles and they correspond to the sequences $\overline{AB^3A^2B^3}$, $\overline{AB^3AB^3A^2B^3}$, and so on. Inside these circles there is actually a continuum of possible circles with a diameter that depends upon the initial conditions. These circles are centered around a single point that corresponds to the periodic orbit that these orbits approach.

As H increases, we remarkably do not find a breakdown from regular to chaotic motion in this system. As described before we see the plot skewed farther to the bottom right with larger H but the topology of the system seems to remain the same. For instance in the lower region of the Poincaré map we see the same patterns of series of circles at all different energies with no sizeable connected areas of chaos. We see the characteristic regions of chaos appearing in the regions between the annulus region and the pretzel regions, but we see little change in the relative sizes of the chaotic regions with H .

When we introduce a negative cosmological constant we see some significant changes in the characteristics of the Poincaré sections shown in figures (10) and (13). First, we see that the asymmetric skewing of the graph to the bottom right is reduced and “pushed” back to the center. Specifically as Λ approaches its negative critical value, the Poincaré section becomes symmetric about the $p_r = 0$ line. In the bottom pretzel region we see that the repeating pattern of circles is continued but again centered on the graph instead of skewed to the right. This is similar to the low energy Newtonian case studied in [8] where the Poincaré section is also centered around $p_r = 0$. This is commensurate with the interpretation that the negative critical value of Λ for a given energy corresponds to the point where all of the energy in the system is vacuum energy, leaving no (ie very little) energy left for the motion of the particles.

The most suprising feature of the Poincaré section when $\Lambda < 0$ is the rapid disappearance of all the regions of chaos. In the region between the annulus and pretzel regions we find that once-chaotic orbits split into purely annulus or purely pretzel class orbits as Λ approaches its negative critical value. We find no evidence of the onset of a KAM breakdown anywhere

Figure 12: The Poincaré plot of the system with $H = 1.5$ and $\Lambda = 0$. The upper inset provides a closeup of the upper chaotic region while the lower inset provides a closeup of the lower right pretzel region.

Figure 13: The Poincaré plot for the system at $H = 1.5$ and $\Lambda = -0.25$, just above the critical value at that energy. The upper inset provides a closeup of the upper chaotic region which has essentially disappeared. The lower inset provides a closeup of the lower right pretzel region.

Figure 14: The Poincaré plot of the system at $H = 1.5$ and $\Lambda = 0.02$, close to the upper limit of Λ that is numerically obtainable.

in the plot. This feature is strikingly different from what we have seen in the corresponding Newtonian system where chaos is present at all energies.

In our study of the $\Lambda < 0$ case we were able to numerically solve the equations of motion of the hex-particle for all values of Λ up to the physical limit of the critical negative value where all of the energy of the system is “used up” in the contraction of the spacetime. However, for the $\Lambda > 0$ case, due to the reduction of V_{rc} as Λ increases (as previously described) we find that the system that was in a perturbative regime quickly changes into an intrinsically nonperturbative system and our numerical simulations break down. This places much greater restrictions on what values of $\Lambda > 0$ we can test, especially at higher energies. Because of this numerical limit, our study of the $\Lambda > 0$ case is somewhat more limited since we cannot follow the changes to this system up to a physical limit. However, we have seen the beginnings of a number of characteristic changes to the Poincaré section as Λ increases, as shown in figures (11) and (14).

First, many features are skewed farther to the right as Λ increases. Furthermore many of the features in the bottom pretzel region seem to be skewed up and to the right instead of down. Below the two large circles in the pretzel region we again see the repeating pattern of circles very well defined.

We also find that the chaotic region in between the boundary of the annulus and pretzel regions is also greatly increased, both in the corners of the boundary and along the sides. These characteristics are found at all numerically obtainable values of H , though for larger H , as described before we cannot increase Λ as much before the system becomes non-integrable.

Furthermore, as Λ increases we at first see the onset of KAM breakdown in the pretzel region, followed by the appearance of major regions of chaos. This transition is illustrated in figure (15). For $H = 1.2$, at $\Lambda = 0.025$ we already begin to see some of the lines widen and small regions of chaos appear between the groups of ellipses. In these narrow regions the hex-particle seems to switch between orbits with an infinitely repeating symbol sequence (which correspond to the groups of ellipses) and orbits which undergo additional A type motions in quasiperiodic intervals (corresponding to the wavy lines) at seemingly irregular intervals. It is these regions that result in the chaotic pretzel orbits mentioned before. However, at this point most of the orbits still show very regular motions. As Λ increases to 0.05 we see these new regions of chaos expand around the groups of ellipses. Once we increase Λ to 0.06 most of the lower region of the Poincaré section becomes chaotic, with only a few non-connected regions of regular motion remaining. This is in sharp contrast with the behaviour of the system as Λ becomes negative, in which no evidence of any KAM breakdown is apparent.

Unfortunately, due to our previously mentioned limitations on studying systems with large cosmological constants, for systems with higher energies we have not been able to numerically investigate systems with as large a value of Λ , so we have not been able to observe this full KAM breakdown at all energies. However, for lower values of Λ we have observed the same initial trends of the lines between the series of ellipses begin to thicken as shown in the lower right insert of figure (14). Figure (16) shows another example of these trends at higher energies. As Λ is increased, we again see an increase in the area of the upper chaotic regions and the appearance of very small regions of chaos in between the series of ellipses. This suggests that the preliminary stages of KAM breakdown occur at these higher energies as well.

Figure 15: A closeup of the pretzel region of the Poincaré plots with $H = 1.2$ for increasing values of Λ . The diagrams are all of the same part of the section. We see clear evidence of KAM breakdown as Λ increases.

Figure 16: Regions of the Poincaré section at $H = 1.8$ and $\Lambda = 0$ for the top graphs and $\Lambda = 0.0085$ for the bottom graphs. The graphs on the left show closeups of the upper chaotic region and the graphs on the right show closeups of the lower pretzel region.

8 Discussion

Our investigation of the cosmological 3-body problem has revealed a number of interesting features. We find in general that the presence of a cosmological constant significantly modifies the chaotic properties of the relativistic 3-body system, and this in markedly different ways depending on its sign.

For a negative cosmological constant we find that there is a rapid decrease in the amount of chaos for all values of H that we were able to investigate. The size of the chaotic regions in the Poincaré plot are even smaller than in its non-relativistic counterpart, despite the high degree of non-linearity in the cosmological system. Indeed, as the cosmological constant approaches its negative critical value (defined in 47), the chaotic regions nearly vanish. We conjecture that this occurs for arbitrarily large H , motivated primarily by our observation that the area of the chaotic regions in the Poincaré section seems to be roughly proportional to $\left| \frac{\Lambda}{\Lambda_{negcrit}} \right|$ for all energies we were able to numerically investigate.

Conversely, we find an increase in the area of chaotic regions in the Poincaré section when the cosmological constant is positive, both in the regions between the annulus and pretzel orbits, and within the regions corresponding to the pretzel orbits. Though we were unable to investigate very large cosmological constants for systems with higher energies, at higher energies, even for the reasonably small positive cosmological we were able to study, we observed the lines in the pretzel regions of the Poincaré section starting to thicken and very small regions of chaos appear between the groups of ellipses, reminiscent of the preliminary stages of KAM breakdown. We therefore conjecture that this increase in chaos occurs for positive Λ at all energies.

We close with some comments on future work. The unequal mass case remains to be explored. While we expect that the general feature of chaos increasing/decreasing with positive/negative Λ will still be present, there could be a number of surprising features in the details relative to the $\Lambda = 0$ case [9]. However our primary limitation has been that of exploring energies that are below the critical value of the potential. This same limitation was present in previous studies of the $\Lambda = 0$ 3-body system [8, 9] – to move beyond it will require employing a time parameter that is not coordinate time, as well as more sophisticated numerical algorithms that avoid instabilities we encountered at higher energies.

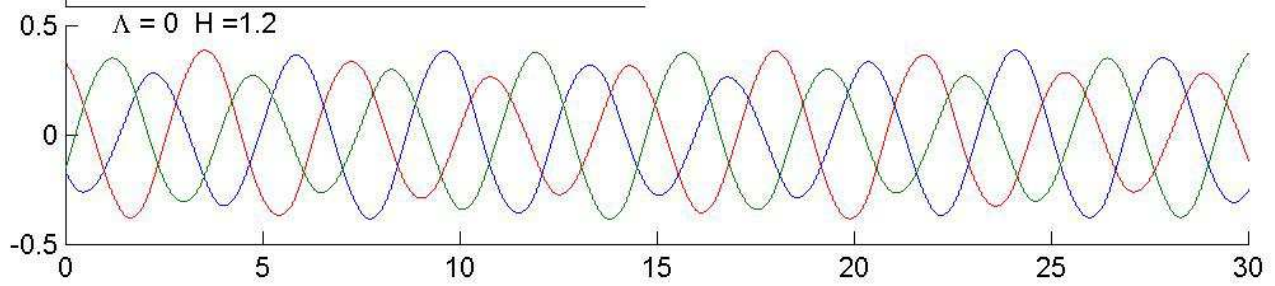
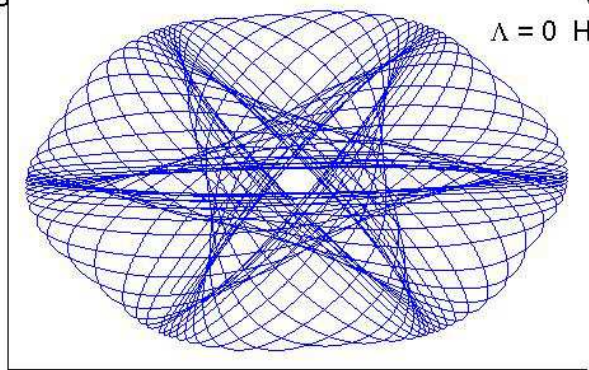
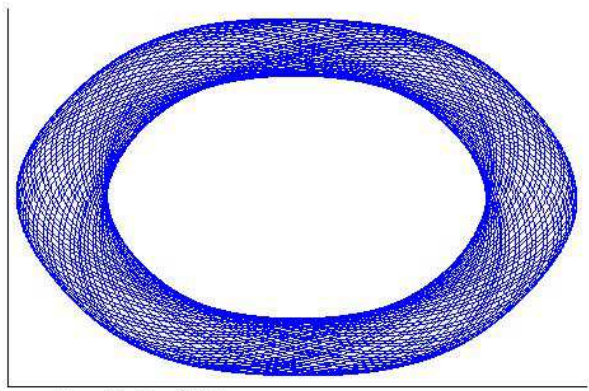
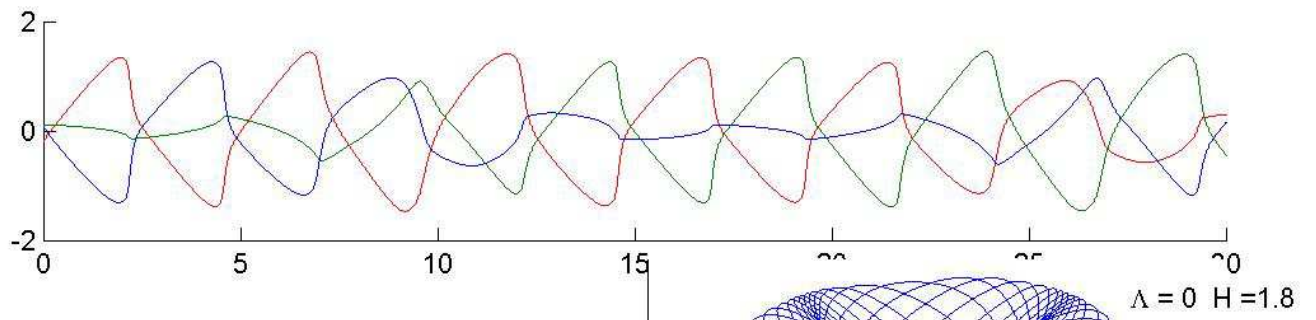
Acknowledgements

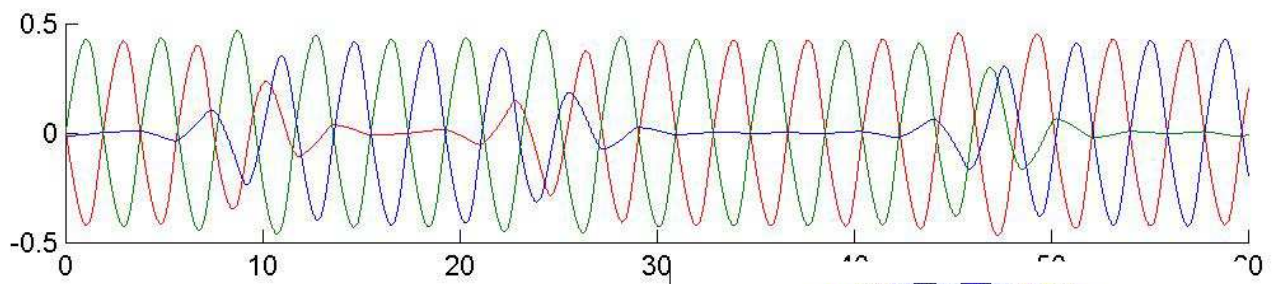
This work was supported by the Natural Sciences and Engineering Research Council of Canada.

References

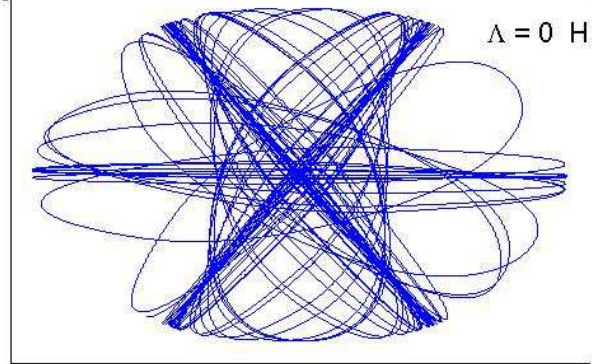
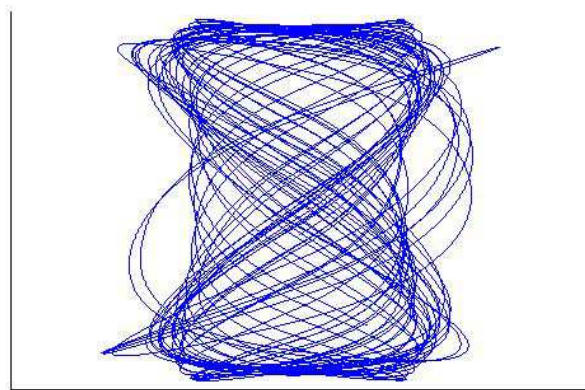
- [1] see the article by T. Damour in Three Hundred Years of Gravitation eds. S.W. Hawking and W. Israel (Cambridge University Press, 1987)

- [2] G. Rybicki, *Astrophys. Space. Sci* **14** (1971) 56; H.L. Wright, B.N. Miller, and W.E. Stein, *Astrophys. Space. Sci.* **84** (1982) 421 and references therein.
- [3] See B.N. Miller and P. Youngkins, *Phys. Rev. Lett.* **81** 4794 (1998); K.R. Yawn and B.N. Miller, *Phys. Rev. Lett.* **79** 3561 (1997) and references therein.
- [4] R.B. Mann, *Found. Phys. Lett.* **4** (1991) 425; R.B. Mann, *Gen. Rel. Grav.* **24** (1992) 433.
- [5] S.F.J. Chan and R.B. Mann, *Class. Quant. Grav.* **12** (1995) 351.
- [6] R. Jackiw, *Nucl. Phys.* **B252**, 343 (1985); C. Teitelboim, *Phys. Lett.* **B126**, 41, (1983).
- [7] F. Burnell, R.B. Mann and T. Ohta, *Phys. Rev. Lett.* **90** (2003) 134101.
- [8] F.J. Burnell, J.J. Malecki, R.B. Mann, and T. Ohta, *Phys. Rev.* **E69** (2004) 016214 .
- [9] J. J, Malecki and R. B. Mann, *IPhys. Rev.* **E69** (2004) 066208.
- [10] R.B. Mann, D. Robbins and T. Ohta, *Phys. Rev.* **D60** (1999) 104048.
- [11] T. Ohta and R.B. Mann, *Class. Quant. Grav.* **13** (1996) 2585.
- [12] R.B. Mann, D. Robbins and T. Ohta, *Phys. Rev. Lett.* **82** (1999) 3738.
- [13] D. Bukta, G. Karl and B. Nickel, *Can J. Phys* **78** (2000) 449.
- [14] H.E. Lehtihet and B.N. Miller, *Physica* **21D** (1986) 93.
- [15] J. L. Rouet, R. Dufour, and M.R. Feix in *Proceedings of the Workshop on Ergodic Concepts in Stellar Dynamics. Geneva, Switzerland (1993)* edited by V.G. Gurzadyan and D. Pfenniger (Springer-Verlag, Berlin, 1994), pp. 193-198.
- [16] V. I. Arnold and A. Avez, *Ergodic Problems of Classical Mechanics* (Springer, New York, 1968); A. N. Kolmogorov, *Dokl. Akad. Nauk SSSR* **98** (1954) 525 [an English version can be found in *Proceedings of the 1954 International Congress of Mathematics (North-Holland, Amsterdam, 1957)*]; V.I. Arnold, *Russ. Math. Surveys* **18** (1963) 85; J. Moser, *Nachr. Akad. Wiss. Goett. II, Math.-Phys. Kl.* **K1** (1962) 1
- [17] H. Koyama and T. Kinoshi, *Phys.Lett.* **A279** (2001) 226; H. Koyama and T. Kinoshi, *Europhys.Lett.***58** (2002) 356.
- [18] H. Reichl and R. Zheng, in *Nonlinear Resonance and Chaos in Directions in Chaos*, edited by B. Hao (World Scientific, Singapore, 1987).
- [19] R.B. Mann and T. Ohta, *Phys. Rev.* **D55** (1997) 4723; *Class. Quant. Grav.* **14** (1997) 1259.
- [20] R.B. Mann, D. Robbins, T. Ohta and M. Trott, *Nucl. Phys.* **B590** 367.

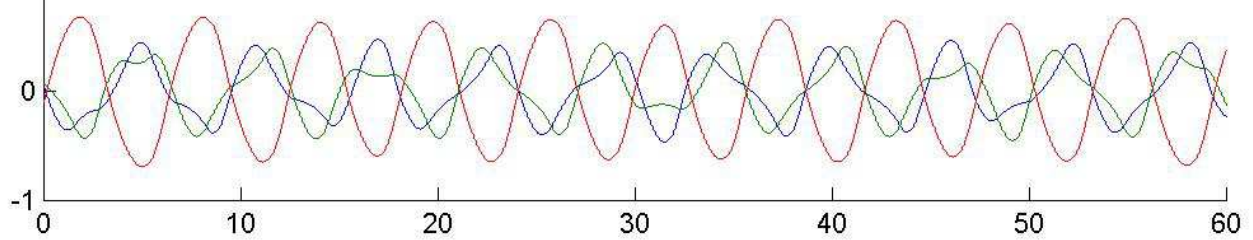


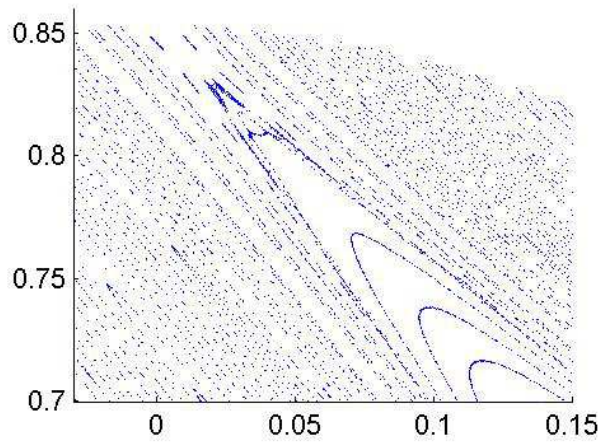


$\Lambda = 0$ $H = 1.2$

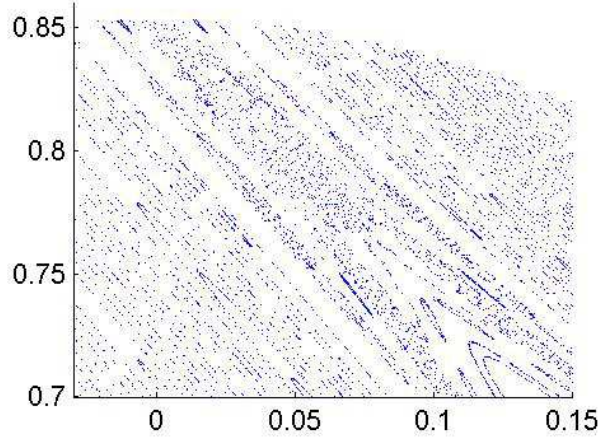
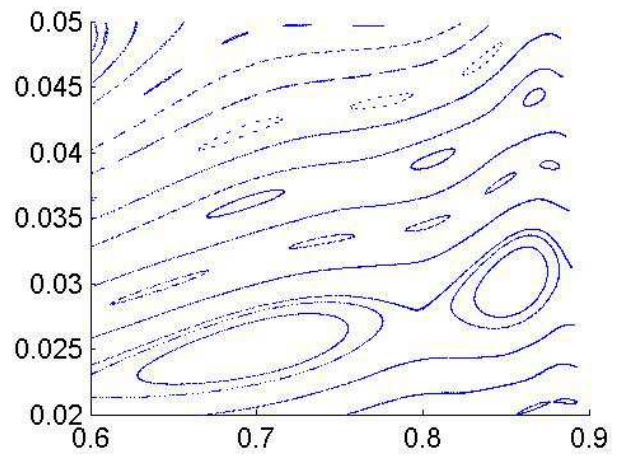


$\Lambda = 0.06$ $H = 1.2$

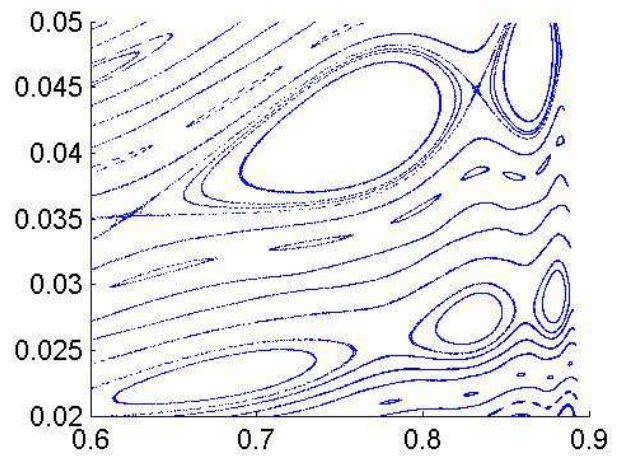


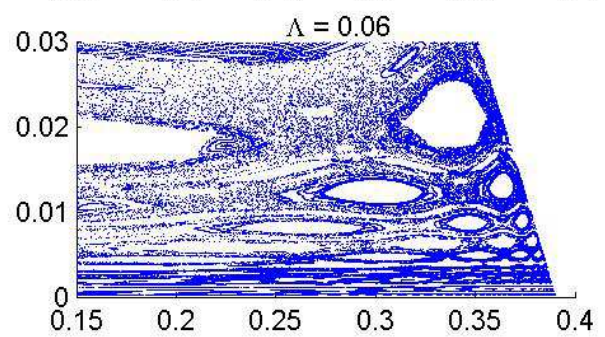
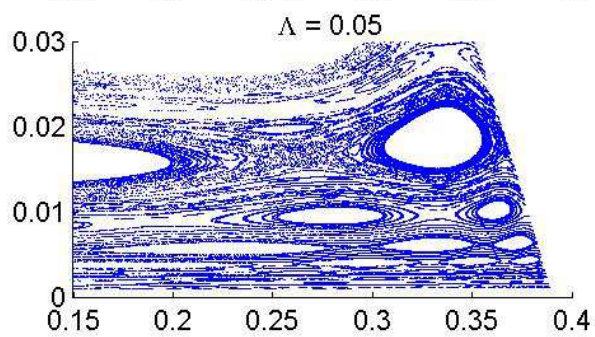
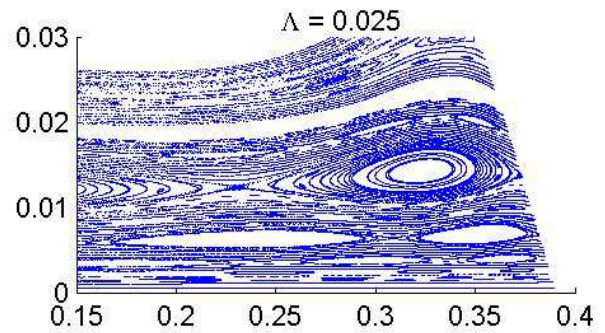
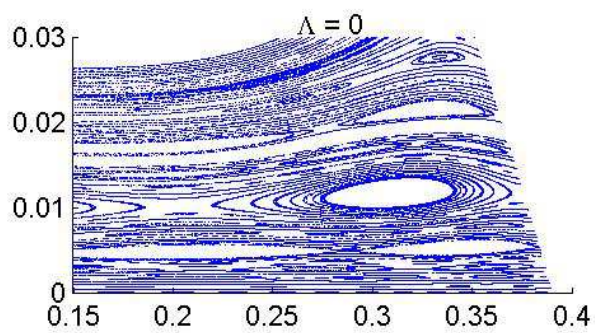
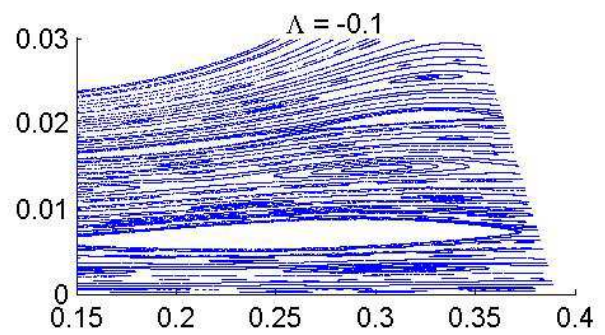
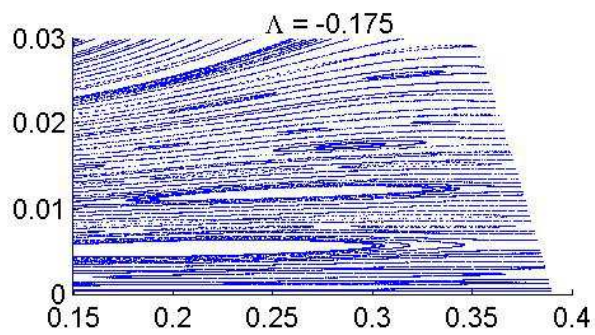


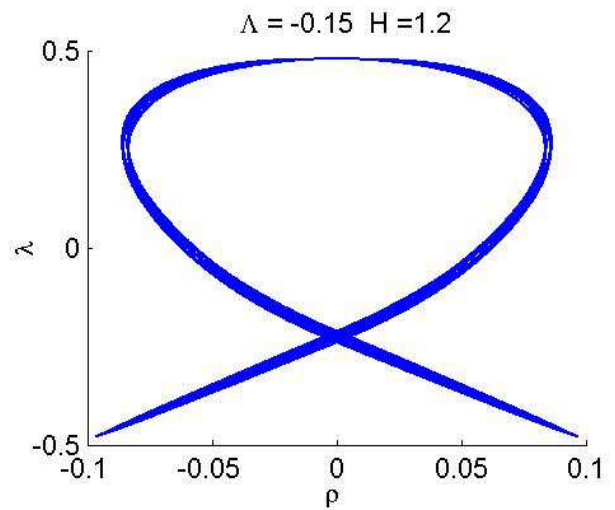
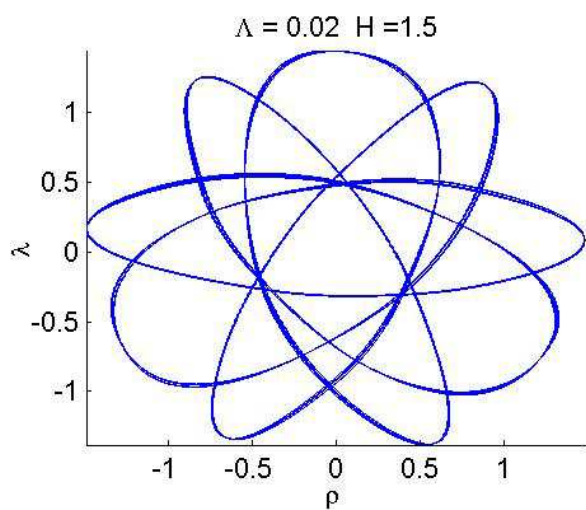
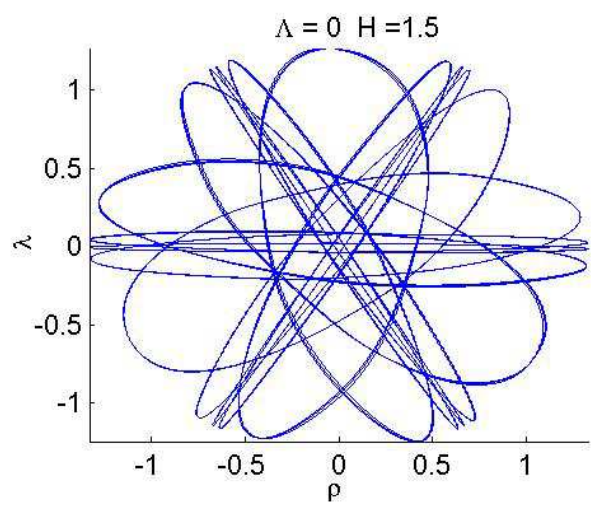
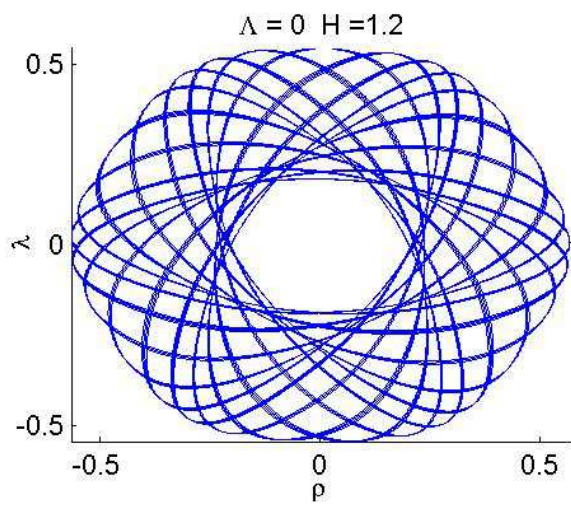
$\Lambda = 0$

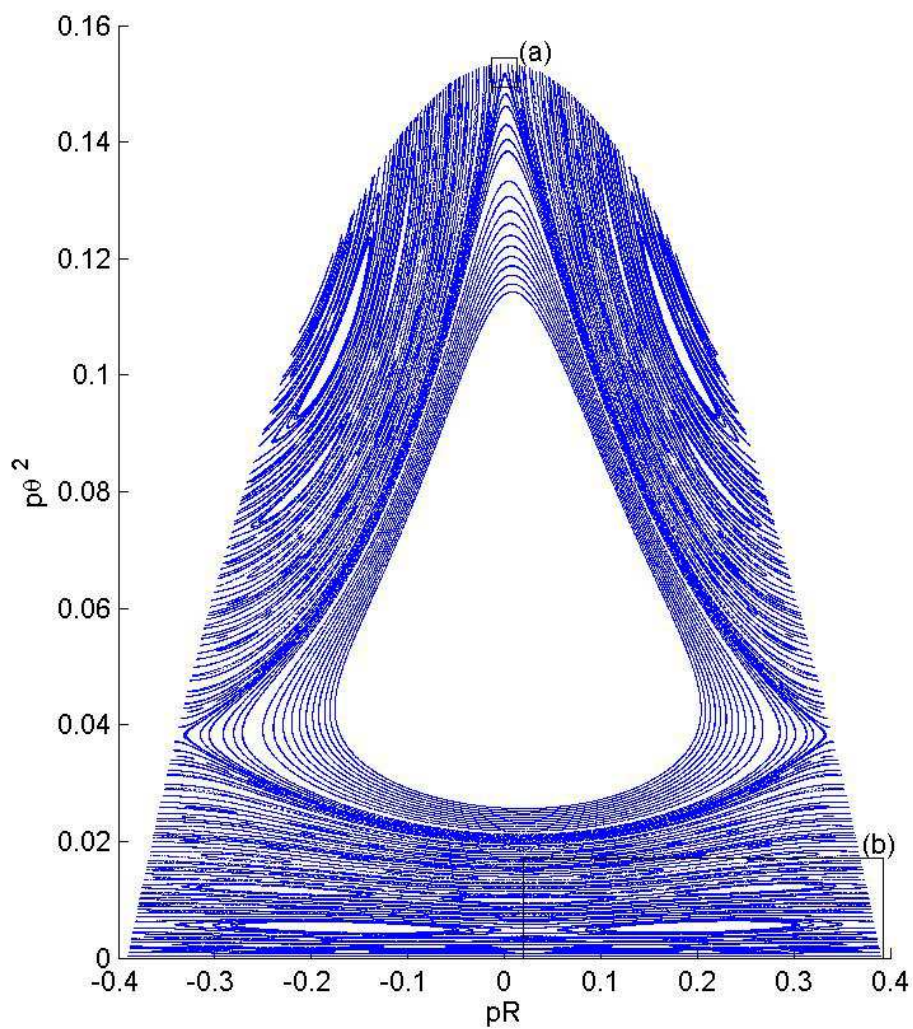


$\Lambda = 0.0085$

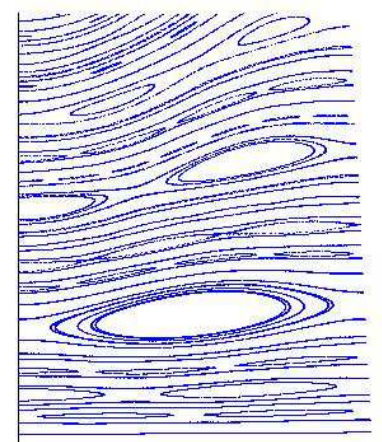
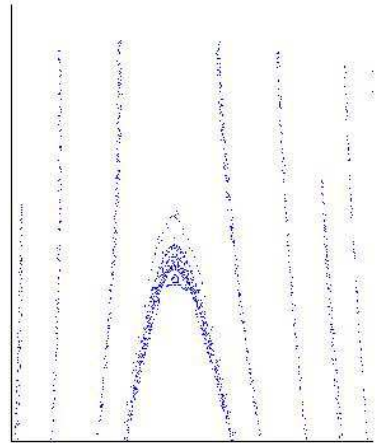




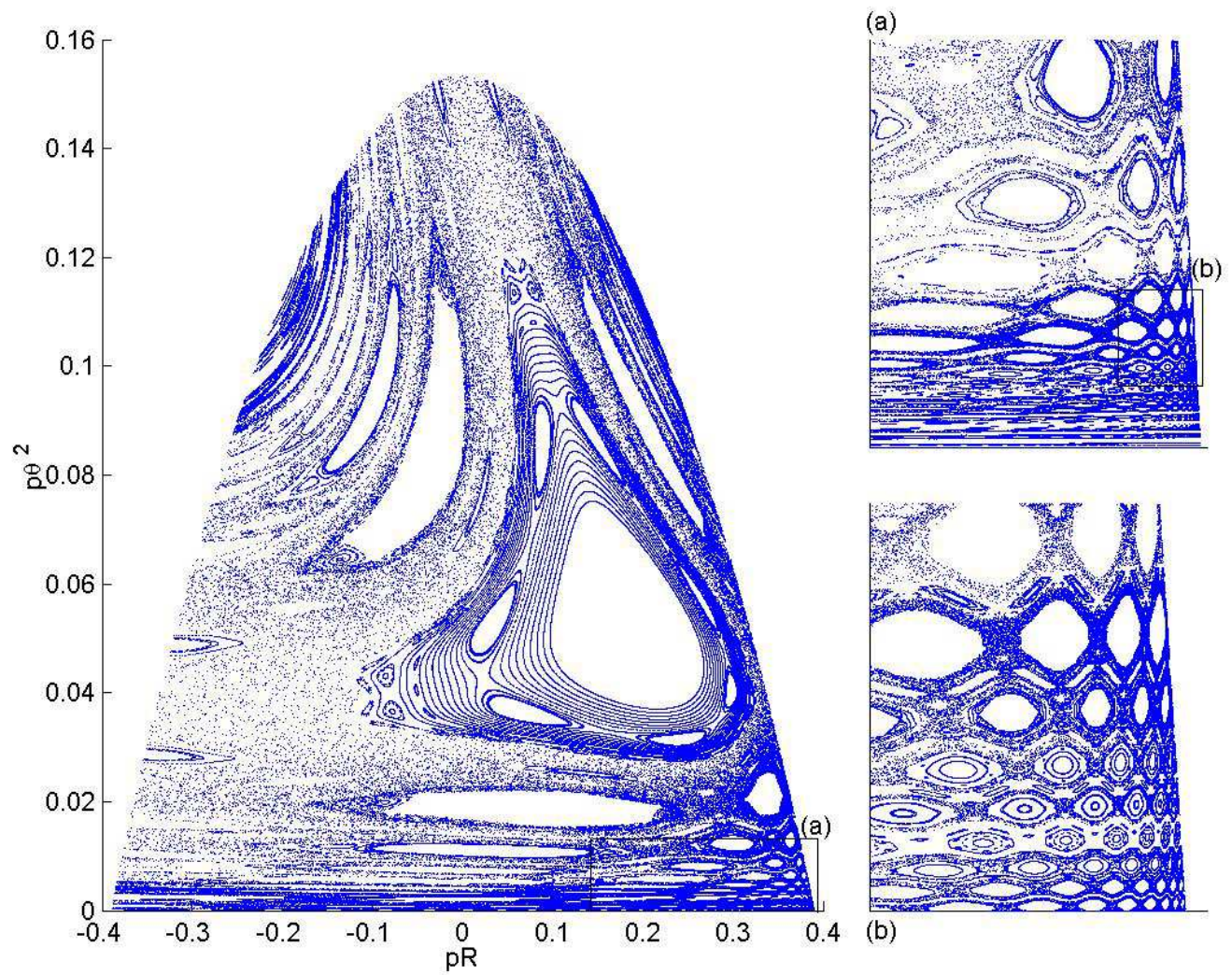


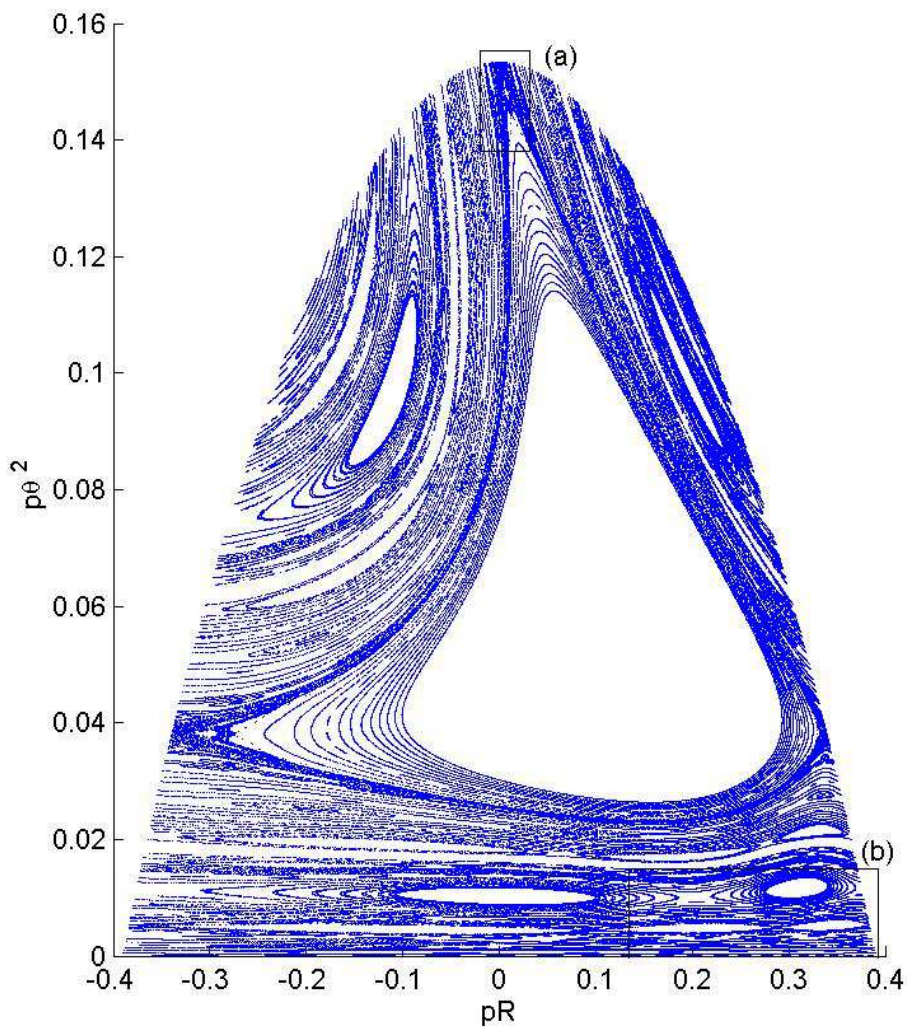


(a) upper chaotic region

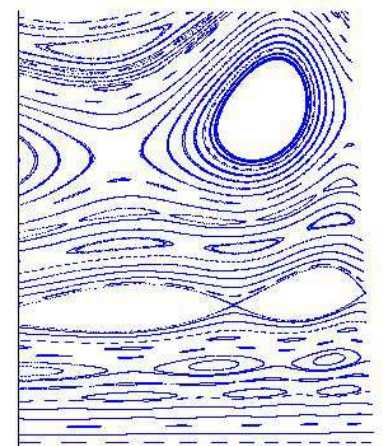
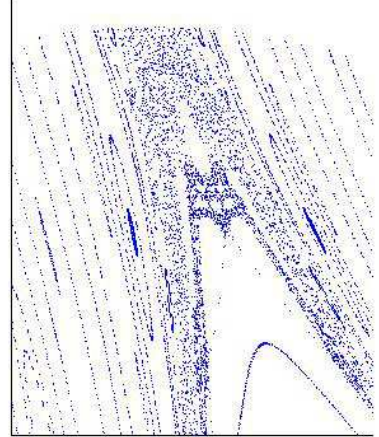


(b) lower right pretzel region

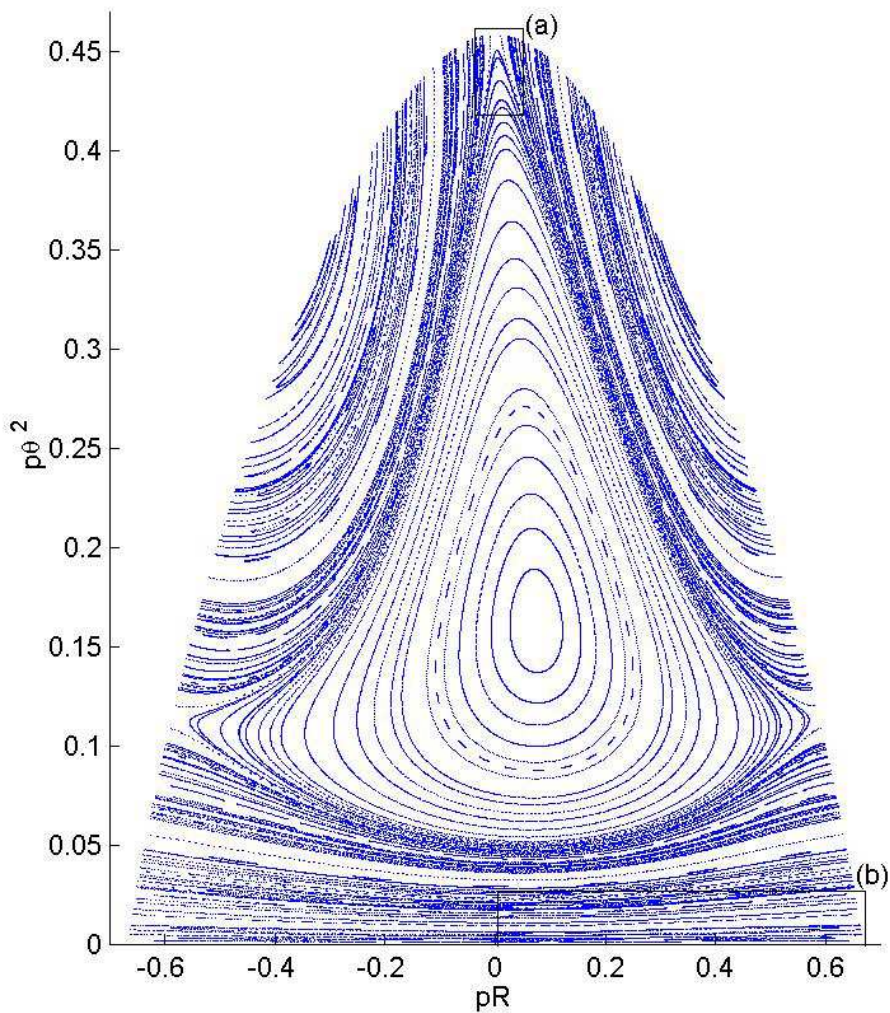




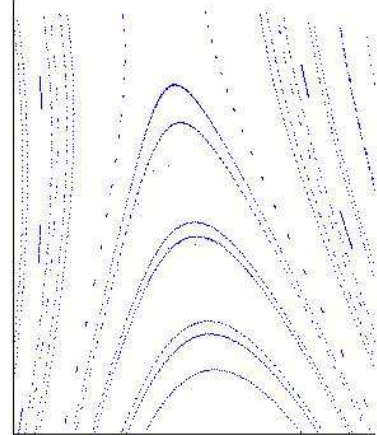
(a) upper chaotic region



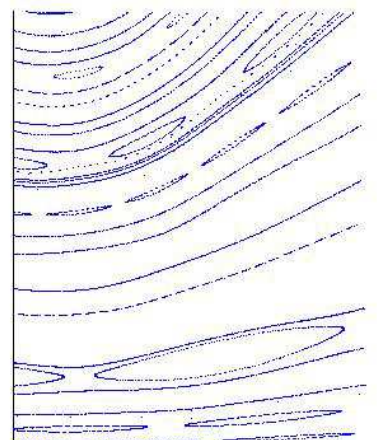
(b) lower right pretzel region

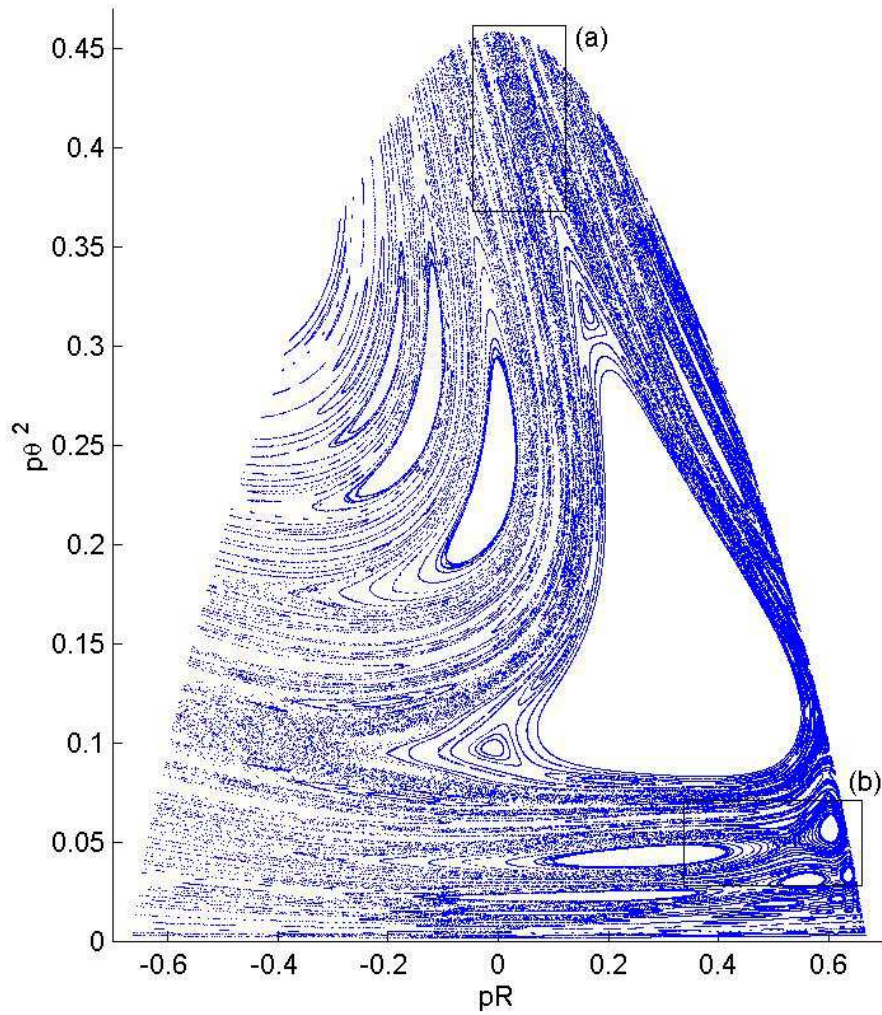


(a) upper region

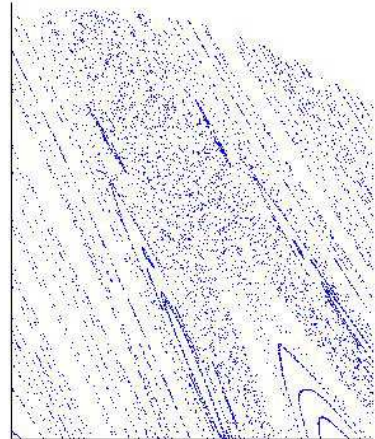


(b) lower right pretzel region

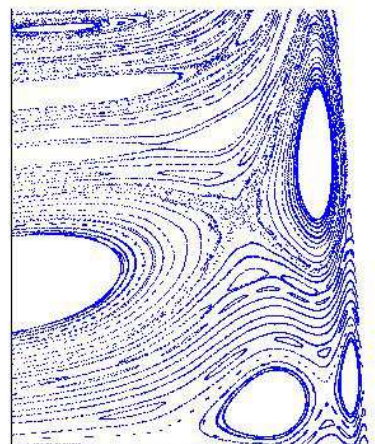


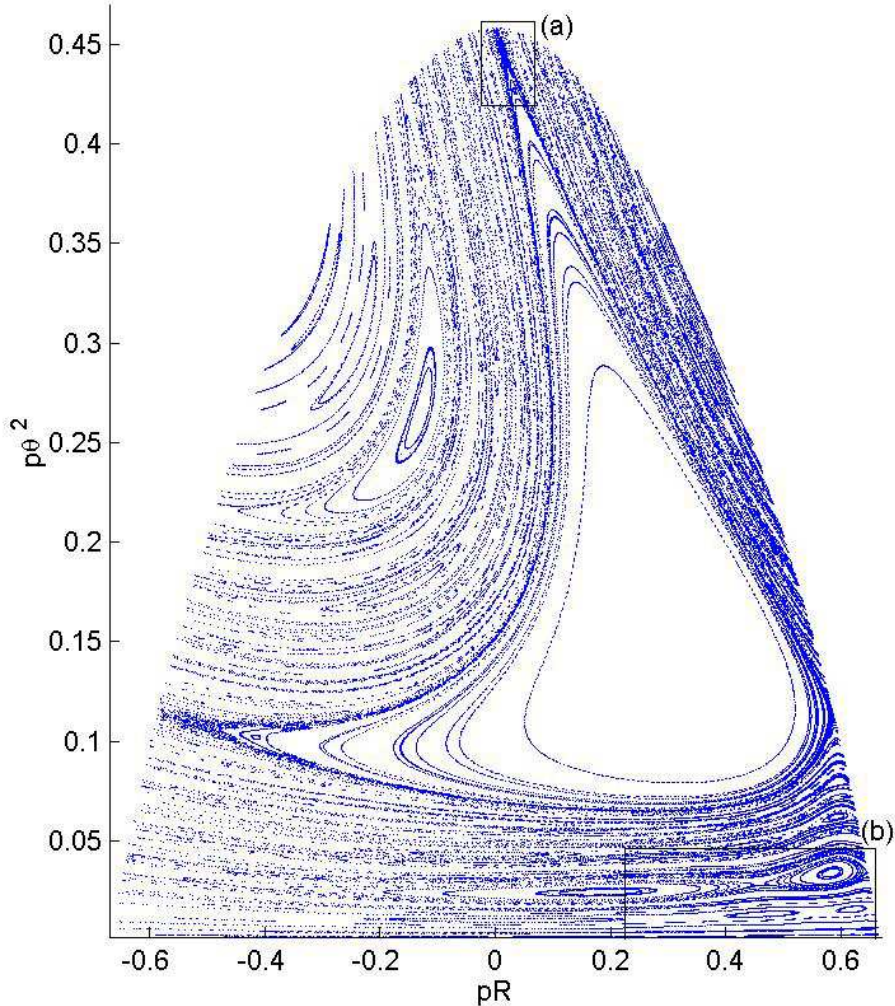


(a) upper chaotic region

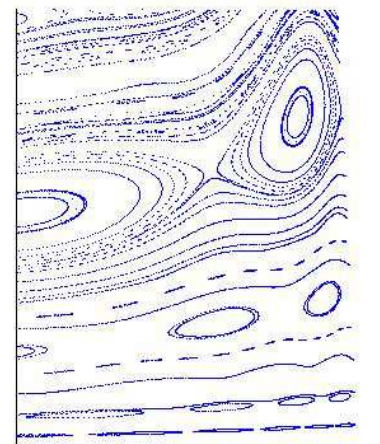
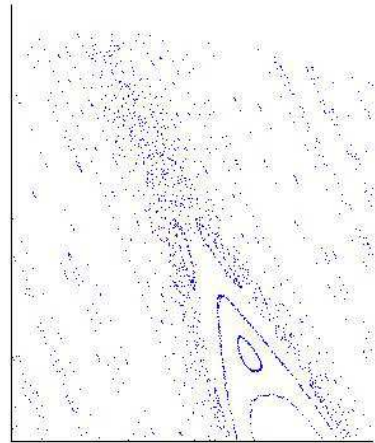


(b) lower right pretzel region





(a) upper chaotic region



(b) lower right pretzel region

